ROYAL SOCIETY OPEN SCIENCE

royalsocietypublishing.org/rsos

CC BY

Research

Cite this article: Bali YB, Rendall A, Quapp W. 2026 Mechanochemical energy landscapes under force support catch–slip bonds in T-cell activation. *R. Soc. Open Sci.* **13**: 252316.
https://doi.org/10.1098/rsos.252316

Received: 5 December 2025
Accepted: 10 June 2026

Subject Category:
Mathematics

Subject Areas:
biomathematics, biochemistry, immunology

Keywords:
T-cell activation, TCR–pMHC recognition, mechanochemical energy landscapes, catch bonds

Author for correspondence:
Yogesh B. Bali
e-mail: ybali@uni-mainz.de

Mechanochemical energy landscapes under force support catch–slip bonds in T-cell activation

Yogesh B. Bali[1], Alan Rendall[2] and Wolfgang Quapp[3]

[1]Institute of Mathematics, Johannes Gutenberg Universitat Mainz, Mainz, Germany
[2]Institut für Mathematik, Johannes Gutenberg Universität Mainz, Mainz, Germany
[3]Mathematisches Institut, Universität Leipzig Fakultät für Mathematik und Informatik, Leipzig, Germany

YBB, 0009-0003-2699-5296; AR, 0000-0003-3666-6632

Traditional theories explain T-cell activation using antigen concentration, binding affinity and dissociation rate, but they fail to account for its extraordinary sensitivity. Recent developments in structural biology, biophysics and modelling have motivated the view that mechanical force can influence T-cell receptor–peptide–major histocompatibility complex (MHC) interactions and reshape receptor–ligand binding under load. We formulate a minimal two-dimensional TCR–pMHC mechanochemical energy-landscape model in which peptide-dependent allosteric binding geometry, hinge elasticity, receptor extension, binding-site separation and applied force jointly determine the activation barrier and bond lifetime. Mathematically, we prove a sharp model-internal force cut-off $F_c = D_0/(2d_0)$—where D_0 is the maximum binding depth and d_0 is the effective interaction-range parameter—above which no bound state exists. At or below this cut-off, the system admits at most two stationary points—a bound minimum and a saddle—which coalesce at the bond-breaking point. Stable binding occurs only on the near-separation branch $d < d_0 \ln 2$. Numerically, we tracked these stationary points under varying force, computed $\Delta E(F)$ and estimated lifetimes using Kramers–Langer theory. Under this peptide-dependent landscape formulation, agonists and weak agonists display catch–slip behaviour, whereas antagonists exhibit slip. This framework provides a phenomenological description of force-dependent TCR–pMHC barrier reshaping and bond lifetimes.

THE ROYAL SOCIETY PUBLISHING

© 2026 The Authors. Published by the Royal Society under the terms of the Creative Commons Attribution License http://creativecommons.org/licenses/by/4.0/, which permits unrestricted use, provided the original author and source are credited.

Downloaded from royalsocietypublishing.org/rsos/article-pdf/doi/10.1098/rsos.252316/6163680/rsos.252316.pdf
by guest
on 02 September 2026

1. Introduction

1.1. Background

The interaction of T-cell receptors (TCRs) with peptides presented by major histocompatibility complex (MHC) proteins is central to cellular immunity. Classical views emphasized receptor–ligand affinity and dissociation kinetics as the primary drivers of T-cell activation. However, TCR–pMHC binding represents one of the weakest protein–protein interactions, with affinities ranging from 10^{-4} to 10^{-6} M—approximately 1000 times weaker than antigen–antibody interactions (10^{-6}–10^{-10} M) [1,2]. Despite this low affinity, TCRs exhibit extraordinary sensitivity and specificity, capable of recognizing a single foreign pMHC among numerous self-antigens in antigen-presenting cells (APCs) [3], and in some settings even responding to a single pMHC [4]. The mechanism behind this high sensitivity, despite weak binding, has been a major focus of research [5].

Several non-exclusive frameworks have been proposed to explain this paradox of high sensitivity and weak binding, including kinetic proofreading, kinetic-segregation or close-contact models, allosteric activation within the TCR–CD3 complex and force-dependent mechanochemical models [6–11]. Accordingly, the molecular basis of TCR triggering remains an active and unresolved area of research. One influential hypothesis is that mechanical forces modulate TCR–pMHC sensitivity and specificity by inducing conformational changes in the receptor–ligand complex, thereby enhancing the ability of the TCR to distinguish between agonist and non-agonist peptides [12]. In line with this view, subsequent work suggested that the $\alpha\beta$ TCR may behave as a mechanosensitive receptor whose response to external load can influence activation [13]. Related theoretical work further proposed that external load may enhance TCR ligand discrimination by altering force-dependent unbinding dynamics and revealing features of the underlying binding-energy landscape [14]. Within the force-based literature itself, however, the consequences of mechanical load for antigen discrimination remain debated, with some studies proposing that force can sharpen ligand discrimination, whereas others suggest that force may instead compress kinetic differences under certain conditions [14,15].

Kim *et al.* [16] provided early experimental evidence that TCRs can respond directly to mechanical load. Using optical tweezers (OT), biomembrane force probes (BFP) and nuclear magnetic resonance (NMR), they reported orientation-dependent engagement and anisotropic force sensitivity of the TCR–CD3 complex. Notably, the application of tangential forces at the level of tens of piconewtons (approx. 10–50 pN) to non-agonist antigens enabled T-cell activation, suggesting that mechanical input can directly contribute to TCR triggering.

This mechanosensitive view was reinforced by Lee *et al.* [17], who showed that T cells bound to artificial APCs expressing elongated anti-CD3 antigens failed to activate in the absence of externally applied force. However, when force was applied, effective T-cell activation occurred, further supporting the view that mechanical transmission through the TCR complex can modulate initiating signalling.

Beyond establishing a role for force in activation, later studies began to address how force may influence antigen discrimination at the level of individual TCR–pMHC bonds. In particular, applying a force of approximately 10 pN was found to prolong the lifetime of bonds formed between TCRs and specific pMHC ligands. Activating peptides formed longer lived bonds under force, whereas antagonist peptides failed to sustain binding under comparable conditions [18,19]. Consistent with this, fluorescence-enabled biomembrane force probe (fBFP) measurements showed that agonist TCR–pMHC interactions can display catch-bond behaviour, in which bond lifetime initially increases with force, thereby extending the time available for productive signalling. By contrast, antagonist ligands form slip bonds, whose lifetimes decrease monotonically with force, limiting downstream activation [20]. This phenomenon, where the lifetimes of the bonds initially increase under applied force, reach a peak at an optimal force level and then decline as the force continues to increase, is referred to as a catch bond [18,21].

In T cells, catch bonds typically peak around 10–15 pN [22]; by contrast, slip bonds weaken as force rises [23,24]. When catch bonds occur, moderate load can extend the contact time between the TCR and the ligand, providing additional time for signalling to occur [25,26]. Such prolonged interactions may, in principle, interface with other proposed triggering mechanisms, including close-contact or protein-segregation models and allosteric structural rearrangements within the TCR–CD3 complex [7,27–29]. In fact, this mechanical force has also been implicated in T-cell development in the thymus, including positive selection [30–32].

Since multiple studies suggest that applying force to TCR–pMHC interactions can prolong bond lifetimes and influence T-cell activation, several mechanisms have been proposed to explain how

Downloaded from royalsocietypublishing.org/rsos/article-pdf/doi/10.1098/rsos.252316/6163680/rsos.252316.pdf
by guest
on 02 September 2026

mechanical load may be converted into productive structural changes at the receptor. A key early event in T-cell signalling is the phosphorylation of tyrosines within immunoreceptor tyrosine-based activation motifs (ITAMs) [33,34]. At a fundamental level, ITAM phosphorylation serves as the principal mechanistic bridge between extracellular (EC) TCR engagement and intracellular T-cell signalling. These ITAMs are present on CD3ε; in resting T cells, the cytoplasmic tails of the TCR complex—particularly CD3ε—are associated with acidic lipids and are embedded in the inner leaflet of the plasma membrane [35]. One proposed mechanism is that antigen engagement, together with local membrane deformation, may generate steric and lateral pressure that promotes conformational rearrangements in the TCR–CD3 complex. Such rearrangements could increase the accessibility of CD3 cytoplasmic tails and thereby facilitate ITAM phosphorylation by lymphocyte-specific protein tyrosine kinase (Lck) [36].

Changes in membrane curvature can also affect lipid packing and may thereby influence TCR signalling dynamics [37,38]. Such structural effects, if present, may also depend on ligand potency, with stronger ligands potentially producing more pronounced rearrangements [39]. Previous theoretical work has shown that catch–slip behaviour can be described through force-dependent reshaping of energy landscapes. Reduced one-dimensional models demonstrate that catch-to-slip switching can arise when structural elasticity and pulling geometry are incorporated [40]. In the TCR–pMHC setting, related modelling studies have connected force-dependent bond lifetimes, energy barriers and antigen discrimination to mechanochemical features of the receptor–ligand interface [21,41]. The present work differs by formulating a two-dimensional TCR–pMHC-specific landscape in which receptor extension and binding-site separation are treated as coupled coordinates.

In this context, the present work examines whether a minimal two-dimensional, ligand-dependent, force-coupled energy landscape can reproduce and help interpret the distinct barrier and bond-lifetime behaviours reported for different classes of TCR–pMHC interactions. In this formulation, ligand identity specifies an allosterically modulated mechanochemical landscape, and applied force subsequently reshapes this landscape by moving minima, saddles and the associated activation barrier. Thus, the model is intended to describe force-dependent TCR–pMHC bond regulation rather than the full process of T-cell activation.

1.2. T-cell receptor structure and how conformational change occurs

The TCR is a heterodimeric glycoprotein composed of α- and β-polypeptide chains (TCR$\alpha\beta$). Each chain has a variable (V) region responsible for antigen recognition and a constant (C) region for structural support. The V region comprises three complementarity determining regions (CDRs), with CDR3 being central to peptide antigen binding. Because the TCR lacks intrinsic signalling capacity, it depends on the CD3 complex for signal transduction [42,43]. The CD3 complex is composed of six non-polymorphic chains, organized into CD3γ–CD3ε and CD3δ–CD3ε heterodimers, along with a CD3$\zeta\zeta$ homodimer, all arranged in specific orientations relative to the TCR [44,45]. A labelled view of the complete TCR–pMHC–CD3 assembly is shown in figure 1.

Recent cryo-electron microscopy (cryo-EM) and molecular dynamics (MD) studies have helped clarify the structural organization, membrane alignment and conformational variability of the TCR–CD3 complex [47–50]. These studies focus on delineating interactions between TCR$\alpha\beta$ and CD3 subunits and on characterizing potential conformational changes in the EC domain of TCR$\alpha\beta$ relative to the membrane. Upon pMHC engagement, these rearrangements couple to the phosphorylation-driven sequence—membrane disengagement of CD3 tails, ITAM exposure and Lck access—outlined in §1.1, thereby linking geometry to early biochemical signalling.

In 2019, single-particle cryo-EM resolved a near-complete human TCR–CD3 complex, including the EC domains and transmembrane (TM) helices, and mapped the chain–chain interfaces [50]. The TCRα chain interacts with CD3δ at the DE loop (the connector between β-strands D and E in the Ig-like Vα domain) and connecting-peptide (CP) region, with additional stabilization from CD3ζ, while the TCRβ chain interfaces with CD3γ and CD3ε mainly in their EC and membrane-proximal segments [50]. Subsequent cryo-EM and NMR studies refined this picture: the TCRα DE loop engages the CD3$\varepsilon\delta$ module, whereas the TCRβ CC′ loop (between β-strands C and C′ in Vβ) contacts both CD3$\varepsilon\delta$ and CD3$\varepsilon\gamma$; by contrast, the TCR Cβ FG loop (between β-strands F and G in the constant β domain) shows only limited interaction with CD3$\varepsilon\gamma$, consistent with cooperative rather than uniformly strong binding across the assembly [51,52].

MD simulations extended these structural findings, revealing broader and more persistent contacts involving the TCR Cβ FG loop (the connector between β-strands F and G in the constant β domain)

Downloaded from royalsocietypublishing.org/rsos/article-pdf/doi/10.1098/rsos.252316/6163680/rsos.252316.pdf
by guest
on 02 September 2026

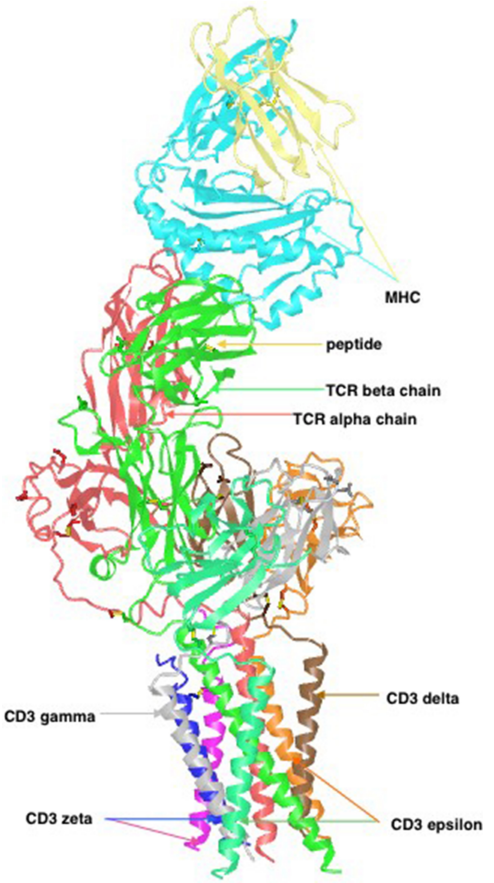


Figure 1. Labelled view of the TCR–pMHC–CD3 assembly. The peptide (gold) lies in the MHC groove, while the MHC is shown at the top in cyan and pale yellow. The TCR β chain is shown in green and the TCR α chain in maroon red. CD3 subunits are coloured as: ϵ (orange), δ (brown), γ (grey) and ζ (purple/blue). Rendered in iCn3D from cryo-EM coordinates (e.g. PDB 8ES8/8ES9); see Saotome *et al.* [46] for experimental details.

and the TCRα variable domain (Vα) than initially appreciated [49]. Notably, comparisons of TCR–CD3 alone with the TCR–CD3–pMHC complex show a marked reduction in TCR–CD3 contacts upon pMHC engagement. This rearrangement is proposed to constrain the spatial freedom of CD3 subunits and to expose or activate signalling motifs within CD3 cytoplasmic tails, thereby initiating downstream signalling and sharpening specificity [7]. Further, the TCR EC domain adopts a bent conformation (approx. 104° tilt) in the resting state and transitions to a more extended orientation (approx. 150°) upon pMHC engagement (see figure 2). This reorganization reorients the TCR relative to CD3, facilitating signal transmission [47,53]. In addition, the CD3ϵ chains exhibit increased flexibility and motion in the presence of pMHC, exploring regions inaccessible in the unbound state [49]. This conformational flexibility supports catch-bond behaviour, akin to selectin catch–slip dynamics, and may enhance the TCR's ability to engage diverse pMHC molecules and transmit activation signals [13,54].

2. Methods

2.1. Model development

Mechanochemistry is an emerging field concerned with how mechanical forces initiate or modulate chemical reactions [55,56]. From a theoretical perspective, an external force perturbs the potential energy surface (PES) of a molecular system, shifting the locations of minima and saddle points (SPs) [57]. These shifts modify the energy barriers separating stable and transition configurations, thereby altering the available reaction pathways. The resulting changes depend on both the magnitude and direction of the applied force [57], which can either enhance or suppress chemical reactivity.

Downloaded from royalsocietypublishing.org/rsos/article-pdf/doi/10.1098/rsos.252316/6163680/rsos.252316.pdf
by guest
on 02 September 2026

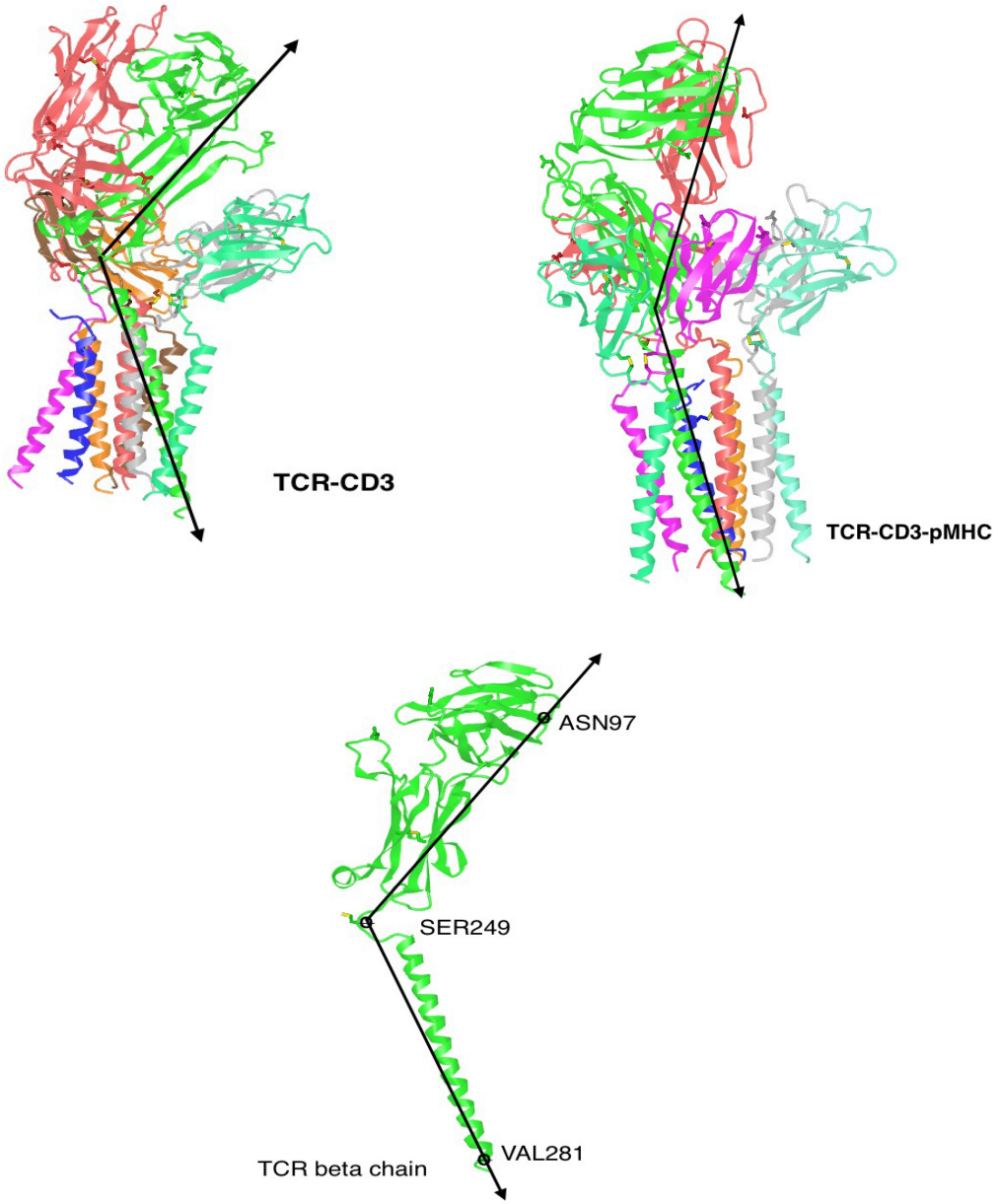


Figure 2. Tilt-angle comparison and definition across the TCR–CD3 assembly. Top left: TCR–CD3 baseline (no pMHC). Top right: pMHC-engaged state (pMHC not shown) with increased TCRβ tilt; same viewing orientation as the left panel for direct comparison. Bottom: residue-based definition of the TCRβ tilt angle θ using ASN_{97}, SER_{249} and VAL_{281}. Other chains are similar to those of figure1.

The catch–slip bond phenomenon provides a prominent example of force-modulated reactivity. In our framework, this behaviour is interpreted as arising from force-induced changes in the PES that generate two effective regimes [58]. At low-to-intermediate forces, load can stabilize the bound configuration relative to the transition state, consistent with a catch-like increase in bond lifetime. At higher forces, however, the same load promotes barrier lowering and bond rupture [59,60], in line with the slip-like behaviour reported for TCR catch bonds.

To capture the dynamics of catch–slip bonds, simplified, coarse-grained models of the PES have been developed. These models provide a clear representation of how mechanical forces affect PES and, in turn, influence bond stability and reaction mechanisms. By incorporating these models, researchers can better understand the interplay among force, energy landscapes and chemical reactivity, providing mechanistic insight into mechanochemistry [61]. As indicated by SMD simulations, as well as studies employing OT [6], BFP, magnetic tweezers [62] and cryo-EM techniques [49], the TCR–pMHC interactions under

Downloaded from royalsocietypublishing.org/rsos/article-pdf/doi/10.1098/rsos.252316/6163680/rsos.252316.pdf
by guest
on 02 September 2026

force are associated with the formation of catch–slip bonds. These studies revealed that the TCR–pMHC complex undergoes elastic expansion as it transitions from the bound state to the transition state. This process is accompanied by structural changes, including hinge rotations and the unfolding of interdomain connections [62]. Specifically, the angle between the TCRβ TM domain and the EC domain increases upon binding with pMHC [47,63], providing the mechanical coupling that links force application to biochemical signalling. Newton trajectory (NT) theory offers a natural way to analyse the force-dependent geometry of the PES [58,64]. On the PES, local minima correspond to stable bound states, whereas SPs represent transition states that must be crossed for dissociation [65]. An applied force shifts both the bound minimum and the transition-state saddle, thereby changing the barrier between them and, in turn, the bond lifetime [66,67]. This is precisely the perspective adopted in our coarse-grained model.

The potential energy landscape of a molecular system under external force, denoted $V_f(\mathbf{x})$, is commonly modelled as [58,64]

$$V_f(\mathbf{x}) = V_0(\mathbf{x}) - F\,\mathbf{f}^{\top}\mathbf{x}, \tag{2.1}$$

where:

— $V_0(\mathbf{x})$ is the intrinsic (unloaded) PES of the system.
— The term $F\,\mathbf{f}^{\top}\mathbf{x}$ represents the effect of a constant force F applied along the unit direction $\mathbf{f}$ (superscript $^{\top}$ denotes transpose) [68].

This framework captures how mechanical loading reshapes the energy landscape and shifts stationary points, including minima and SPs, in configuration space [65,69]. If $\mathbf{x}_m(F)$ denotes a local minimum and $\mathbf{x}_s(F)$ the adjacent SP on the loaded surface, then the corresponding force-dependent barrier is defined as

$$\Delta E(F) = V_f(\mathbf{x}_s(F)) - V_f(\mathbf{x}_m(F)). \tag{2.2}$$

Equivalently, substituting the expression for V_f gives

$$\Delta E(F) = V_0(\mathbf{x}_s(F)) - V_0(\mathbf{x}_m(F)) - F\,\mathbf{f}^{\top}\big(\mathbf{x}_s(F) - \mathbf{x}_m(F)\big), \tag{2.3}$$

showing that the barrier consists of the intrinsic PES contribution corrected by the force-induced energy shift.

At stationary points $\mathbf{x}_c$, the gradient of the effective PES vanishes, which leads to

$$\mathbf{g}(\mathbf{x}_c) := \nabla V_0(\mathbf{x}_c) = F\,\mathbf{f}, \tag{2.4}$$

where $\mathbf{g}(\mathbf{x}_c)$ is the gradient of the intrinsic PES [57]. Curves satisfying this relation for varying F are NTs. For any $\mathbf{x}_c$, the corresponding force magnitude is

$$\|\mathbf{g}(\mathbf{x}_c)\| = \big(\mathbf{g}^{\top}(\mathbf{x}_c)\mathbf{g}(\mathbf{x}_c)\big)^{1/2}. \tag{2.5}$$

These trajectories describe how molecular configurations evolve with applied force. To describe the motion of any critical point $\mathbf{x}_c$, we formulate a corresponding differential equation:

$$\frac{\mathrm{d}\mathbf{x}_c}{\mathrm{d}t} = \mathrm{Det}(\mathbf{H})\mathbf{H}^{-1}(\mathbf{x}_c)\mathbf{g}(\mathbf{x}_c).$$

Here, $\mathbf{H}^{-1}$ denotes the inverse of the Hessian matrix associated with the intrinsic PES, and $\mathrm{Det}(\mathbf{H})$ represents the determinant of this matrix. The variable t is a parameter along the NT [70,71]. To suppress Hessian singularities, a regularized matrix $\mathbf{A}$ is defined as

$$\mathbf{A} = \mathrm{Det}(\mathbf{H})\,\mathbf{H}^{-1}.$$

NTs structurally link minima to first-order SP1s, which correspond to transition states in chemical systems [72–74]. Each NT intersects points where

$$\mathrm{Det}(\mathbf{H}) = 0, \tag{2.6}$$

signalling the coalescence of a minimum and SP, termed the bond-breaking point (BBP) [64].

Downloaded from royalsocietypublishing.org/rsos/article-pdf/doi/10.1098/rsos.252316/6163680/rsos.252316.pdf
by guest
on 02 September 2026

In the context of TCR–pMHC interactions, the structural interplay between the hinge angle and the binding interface, as previously discussed, plays a pivotal role in modulating the thermodynamic and kinetic properties of molecular recognition. This interaction is characterized by the nonlinear coupling between the binding-interface separation (d) and the conformational dynamics of the protein complex. Consequently, the free-energy landscape, which governs both equilibrium states and transition pathways, is primarily described in terms of two independent but energetically coupled coordinates: the protein extension (L) and the ligand-binding site distance (d). This construction allows force to reshape both receptor geometry and interfacial separation, and provides the coordinate structure used below to track force-dependent minima, saddles and BBPs. The corresponding geometry (θ, L, d) is illustrated in figure 3.

To enhance analytical tractability, TCRβ extension, denoted as $L(\theta)$, serves as a surrogate variable for the hinge angle (θ), thereby circumventing the need for explicit angular parametrization. This substitution exploits the geometric dependency between L and θ, which adheres to the functional relationship

$$L(\theta) = 2W \sin\left(\frac{\theta}{2}\right),$$

and inversely,

$$\theta(L) = 2 \arcsin\left(\frac{L}{2W}\right).$$

Here, W represents the effective length of the TCR complex, estimated at 7 nm [48]. These relationships streamline the representation of the free-energy landscape while preserving the essential coupling between conformational dynamics and binding energetics.

The total free energy of the TCR–pMHC system, denoted as $V_f(L, d)$, accounts for intrinsic hinge energetics, ligand binding interactions and external force contributions:

$$V_f(L, d) = V(\theta(L)) + B(d, \theta(L)) - (L + d)F, \tag{2.7}$$

where each term represents a distinct energetic component governing TCR–pMHC interactions [68,75].

The hinge energy $V(\theta(L))$ describes the system's preference for a specific hinge angle, modelled using a harmonic potential:

$$V(\theta) = \frac{1}{2}k_\theta(\theta - \theta_0)^2. \tag{2.8}$$

Here, k_θ is the effective angular stiffness of the bound TCR–pMHC complex, quantifying resistance to deviation from the equilibrium angle θ_0, found to be approximately 0.60π radians [47]. The quadratic term penalizes deviations from θ_0, influencing the conformational stability of the bound receptor–ligand complex [76].

The ligand binding energy $B(d, \theta(L))$ characterizes the interaction between the TCR–pMHC complex, modelled by a Morse potential:

$$B(d, \theta) = D(\theta)\left[\left(1 - e^{-d/d_0}\right)^2 - 1\right]. \tag{2.9}$$

Here, $D(\theta)$ is an angle-dependent binding strength modulating the potential well depth, while d_0 sets the characteristic interaction range of the Morse potential along the separation coordinate [77]. The Morse term therefore captures how binding weakens nonlinearly as the interface is displaced away from the bound-state contact geometry.

The function $D(\theta)$ reflects allosteric modulation of binding affinity and is given by

$$D(\theta) = D_0 \exp\left[-\frac{(\theta - \theta_1)^2}{2\sigma^2}\right]. \tag{2.10}$$

In this formulation, D_0 is the maximum binding strength, θ_1 is the preferred hinge orientation for binding, and σ sets how sharply $D(\theta)$ decays away from θ_1 [78]. Thus, $V(\theta)$ captures the intrinsic energetic cost of hinge bending about the resting angle θ_0, whereas $D(\theta)$ modulates how strongly binding is favoured at different receptor orientations. The term $(L + d)F$ represents the mechanical work of an applied load

Downloaded from royalsocietypublishing.org/rsos/article-pdf/doi/10.1098/rsos.252316/6163680/rsos.252316.pdf
by guest
on 02 September 2026

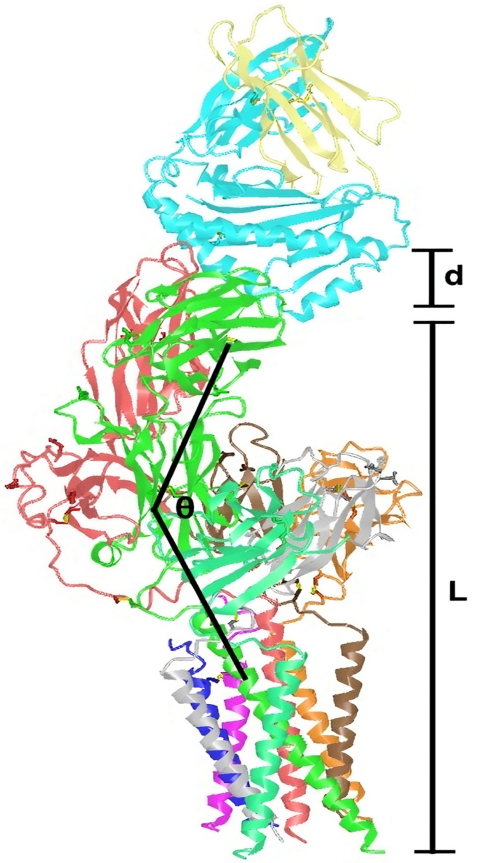


Figure 3. Geometric definitions used in the model. The hinge angle θ (black arc) is defined at the TCR hinge, L denotes the axial distance from the CD3 TM region to the TCR–pMHC interface, and d represents the binding-site separation along the pulling axis. These coordinates, (L, d, θ), enter the free-energy formulation in equation (2.7).

F, which effectively modulates both the extension L and the ligand distance d, thereby reshaping the binding landscape [68].

In practice, F denotes the effective piconewton force transmitted along the pulling direction of the TCR–pMHC–CD3 complex, arising from processes such as actin–myosin activity, membrane deformation or microvillus scanning. In the present coarse-grained description, this force enters the PES as a linear tilt, $-F\,\mathbf{f}^{\top}\mathbf{x}$, with $\mathbf{x}^{\top} = (L, d)$, thereby capturing how force shifts minima and SPs without requiring a detailed specification of its microscopic origin. In the TCR-specific model considered here, this corresponds to the term $-(L + d)F$, that is, equal projection of the effective force onto the extension and separation coordinates. The constant-load (force-clamp) approximation is consistent with BFP/OT-type conditions, while the chosen pulling direction provides a simplified representation of receptor loading under traction. With parameters calibrated to measured piconewton ranges, this formulation isolates the effect of force on the energy landscape—specifically, the displacement of minima and saddles—without committing to a single microscopic source of the load.

2.2. Mathematical analysis

We analyse the stationary conditions for bound configurations of the total free-energy landscape. This analysis yields results on the existence, multiplicity and local stability of stationary points under force. Here, we summarize only the analytical conclusions most relevant for interpreting the force-dependent energy landscape. The formal mathematical statements are collected in appendix C, while the full derivations are provided in the supplementary material.

Downloaded from royalsocietypublishing.org/rsos/article-pdf/doi/10.1098/rsos.252316/6163680/rsos.252316.pdf
by guest
on 02 September 2026

2.2.1. Existence and multiplicity of stationary points

The stationary-point analysis gives the following results. (i) Bound stationary configurations can exist only when the applied force satisfies

$$F \le F_c := \frac{D_0}{2d_0}.$$

For $F > F_c$, the loaded free-energy landscape admits no bound stationary points. Thus, F_c is an existence threshold of the reduced energy landscape, corresponding to the fold at which the bound minimum and adjacent saddle cease to exist as distinct stationary configurations. (ii) When $F \le F_c$, the stationarity conditions reduce to a scalar condition in the angular variable, from which it follows that the number of stationary points is at most two. (iii) For generic parameter values, the number of stationary points is either 0 or 2; single-point cases arise only in degenerate parameter regimes.

2.2.2. Local stability of stationary points

To determine which stationary points correspond to physically admissible bound configurations, we next analyse the Hessian of the loaded free-energy landscape. The Hessian analysis shows that only the near branch,

$$u^* > \tfrac{1}{2} \qquad \left(\text{equivalently } d^* < d_0 \ln 2\right),$$

can satisfy the necessary positive-curvature condition along the separation coordinate d. A stationary point is therefore classified as a strict local minimum only when the Hessian is positive definite, that is,

$$H^*_{dd} > 0, \qquad \det H^* > 0.$$

If $\det H^* < 0$, the stationary point is a saddle, whereas $H^*_{dd} < 0$ implies instability along d. In particular, at the fold $u^* = 1/2$, one has $H^*_{dd} = 0$, so no strict local minimum can occur there. Thus, the Hessian analysis distinguishes force-supported bound minima from nearby saddle configurations that define the escape pathway towards dissociation. Biologically, these results show that applied force does not merely perturb an existing TCR–pMHC bond, but regulates the existence, multiplicity and mechanical stability of admissible bound configurations. Thus, force constrains the set of receptor–ligand states available under load and, in doing so, helps govern whether the complex remains in a stable bound configuration or proceeds towards dissociation.

2.3. Parameter calculations

We quantify binding strength as a positive well depth D_0 (per molecule). For each peptide–TCR pair, D_0 is obtained from its 3D dissociation constant K_D via the standard-state relation

$$\frac{D_0}{k_B T} = -\ln\!\left(\frac{K_D}{1\ \mathrm{M}}\right), \tag{2.11}$$

where ln is the natural logarithm, 1 M is the standard state and T is the assay temperature (we use $T = 310$ K). When a molar free energy is reported instead, we use the equivalent one-molecule definition $D_0 = -\Delta G^\circ / N_A$. We report D_0 both as the dimensionless ratio D_0/k_BT and in pN nm using 1 pN nm = 10^{-21} J; at $T = 310$ K, $k_BT = 4.28$ pN nm. At $T = 310$ K, the corresponding D_0/k_BT values are 12.0 (agonist), 9.4 (weak) and 7.35 (antagonist). This sign convention matches our energy landscape: larger D_0 corresponds to a deeper potential well and stronger binding.

In practice, K_D (and therefore D_0) is ligand-specific even within the same functional class. Accordingly, we compute D_0 per peptide and use class labels (agonist, weak/partial agonist, antagonist) only to summarize the resulting distributions (median and interquartile range). To avoid cross-study mixing of energy scales, our main parametrization relies exclusively on 3D (solution) affinities from the same experimental sources for each dataset.

Consistent with prior measurements of TCR–pMHC affinities [79–81], the per-ligand D_0 values in our 3D compilations fall into characteristic ranges: agonists typically approximately 48–55 pN nm, weak/partial agonists approximately 38–41 pN nm and antagonists approximately 31–35 pN nm. For

Downloaded from royalsocietypublishing.org/rsos/article-pdf/doi/10.1098/rsos.252316/6163680/rsos.252316.pdf
by guest
on 02 September 2026

concreteness, we include representative ligands across this spectrum—gp33-wt (agonist) [79], Y4A (weak agonist) [81] and Y4SC9M (antagonist) [81]. Here, D_0 represents an effective one-coordinate well depth along the ligand separation axis that reproduces the measured three-dimensional free energy ΔG° after integrating out other degrees of freedom, thereby ensuring thermodynamic–mechanical consistency in our parametrization. Full per-ligand conversions ($\Delta G \to D_0$) and class summaries for each dataset are provided in the supplementary material.

The angular stiffness k_θ sets the energetic penalty for deviations of the bound TCR–pMHC complex from its preferred hinge orientation and serves as an effective coarse-grained measure of angular rigidity in the model. Since no direct ligand-resolved measurements of this quantity are available for the present systems, we estimated k_θ phenomenologically by fitting a unified nonlinear model to published TCR–pMHC bond lifetimes as a function of applied force [6]. The resulting estimates were 76.3 [72.8, 79.7] pN nm for agonists, 80.9 [73.8, 88.0] pN nm for weak agonists and 85.3 [61.6, 109.1] pN nm for antagonists, where brackets denote bootstrap confidence intervals. The fitted values suggest lower effective angular stiffness—and therefore greater angular compliance—in stimulatory complexes, with progressively stiffer angular potentials towards weaker and antagonistic ligands [82]. This ligand-class dependence represents an effective change in the angular rigidity of the bound receptor–ligand complex within the coarse-grained landscape. Because k_θ is inferred from force–lifetime data within a coarse-grained fitting framework, it should be regarded as an effective model parameter rather than a directly measured structural constant. Additional fitting constraints and implementation details are given in the supplementary material.

In this interpretation, the energetic depth and the angular response of the complex play complementary roles. The parameter D_0 sets the depth of the binding well, whereas k_θ and the angular-width parameter σ shape the rigidity and tolerance of the complex under load. A deeper binding well can therefore increase stability without necessarily implying a more compliant force response.

We model the angle dependence of the binding depth as

$$D(\theta) = D_0 \exp\left[-\frac{(\theta-\theta_1)^2}{2\sigma^2}\right],$$

where σ sets the intrinsic angular tolerance of the binding interaction.

We model the angle dependence of the binding depth as

$$D(\theta) = D_0 \exp\left[-\frac{(\theta-\theta_1)^2}{2\sigma^2}\right], \tag{2.12}$$

where σ sets the intrinsic angular tolerance of the binding interaction (smaller σ = sharper selectivity near θ_1; larger σ = broader tolerance). Because the observed bound spread also reflects hinge elasticity (near the minimum, the effective curvature is $\kappa_{\mathrm{eff}} = k_\theta + D_0/\sigma^2$), we do not identify σ directly with an experimentally measured bound full width at half maximum (FWHM); instead, experimentally motivated angular widths are used only as calibration anchors.

The angular width parameter σ defines the effective angular tolerance of the TCR–pMHC interface and directly modulates the breadth of the binding potential $D(\theta)$. To parametrize this quantity consistently across ligands, we first relate experimentally observed angular spreads to model parameters and then link them to binding thermodynamics.

For each dataset, we define a reference width σ_0 from referenced strong agonist (C9L, $\Delta G_0 = -7.00$ kcal mol^{-1} [81]) by converting a simulation-derived angular spread to a Gaussian standard deviation:

$$\sigma_0 = \frac{\mathrm{FWHM}}{2\sqrt{2\ln 2}} \approx \frac{\mathrm{FWHM}}{2.3548}. \tag{2.13}$$

Coarse-grained MD simulations of the pMHC-engaged TCR–CD3 complex report a FWHM of approximately 30° for the TCR EC domain tilt angle in the bound state [47], giving $\sigma_0 \simeq 0.222$ rad. We treat this value as a structurally generic property of $\alpha\beta$ TCRs engaged with agonist pMHC, rather than as a C9L-specific measurement.

To account for ligand-dependent variability within a given dataset, we scale σ monotonically with the molar binding free energy (ΔG) using Boltzmann-type scaling:

$$\sigma = \sigma_0 \exp\big[\gamma\,(\Delta G - \Delta G_0)\big], \tag{2.14}$$

Downloaded from royalsocietypublishing.org/rsos/article-pdf/doi/10.1098/rsos.252316/6163680/rsos.252316.pdf
by guest
on 02 September 2026

where ΔG_0 is the free energy of the reference agonist and γ has units $(\text{kcal mol}^{-1})^{-1}$. This form reflects the expected statistical–mechanical link between energetic stability and configurational flexibility [83–85]. The parameter γ is determined within each dataset by anchoring the antagonist endpoint to FWHM = 65° ($\sigma_{\text{ant}} = 0.482$ rad), consistent with partial pMHC engagement. Atomistic MD simulations of the unbound TCR–CD3 complex report tilt angles spanning 15°–55° in the absence of pMHC [49], whereas agonist engagement narrows this distribution to FWHM approximately 30° [47]; the antagonist value therefore lies between these limits. The ΔG values are taken directly from the experimental sources reporting the corresponding peptide–MHC interactions [79,81]. Full calibration details are provided in the supplementary material.

The angle θ_1 denotes the reference or central angle at which the binding strength function $D(\theta)$ reaches its maximum. It corresponds to the optimal angular configuration of the receptor–ligand complex, representing the orientation that yields the strongest interaction. This central angle thus defines the most favourable geometrical alignment for productive binding. Deviations from θ_1 lead to a reduction in binding strength, with the rate of decay modulated by the spread parameter σ, which governs the system's angular tolerance. Using the extension–angle relation $\theta_1 = 2\arcsin(L_{\text{bound}}/2W)$ with $W = 7$ nm [50], the resulting angular preferences were set to $\theta_1/\pi = 0.83$ (agonist), 0.80 (weak agonist) and 0.72 (antagonist), reflecting progressively more closed hinge conformations across the affinity series. These choices are consistent with coarse-grained MD simulations of the pMHC-engaged TCR–CD3 complex reporting a peak tilt angle of approximately 150° [47]. Notably, the weak agonist value ($\theta_1 \approx 144°$) coincides with the TCR EC domain tilt angle observed directly in the cryo-EM structure of the TCR–CD3 complex [50], providing independent structural support for this choice.

Experimental work shows that, upon engagement with pMHC, the TCR–CD3 complex adopts a more extended, open conformation, with peak interactions typically near 150° [47]. To compare directly with these observations, we measured the TCRβ tilt angle in unbound and pMHC-bound states using two high-resolution cryo-EM structures: the unbound TCR from Dong *et al.* [50] and the pMHC-bound complex from Saotome *et al.* [46]. For consistency, the hinge angle was defined by the same three residues in both structures—VAL_3, GLY_{164} and ARG_{289}—taken as the angle subtended by VAL_3–GLY_{164}–ARG_{289}. Using UCSF Chimera [86], we obtained a tilt of 104.99° in the unbound state and 147.56° in the pMHC-bound state, indicating a substantial opening upon antigen engagement (figure 9 in appendix B). This shift is consistent with Eerden *et al.* [47], who report a more extended TCR configuration near 150°. All structures were retrieved from the National Library of Medicine Protein Data Bank [87]. Moreover, the magnitude of this conformational change appears to correlate with antigen potency: strong agonists tend to induce larger extensions than weaker ligands, in line with enhanced binding specificity and mechanical stabilization.

The parameter W denotes the effective geometric length scale of the TCR–CD3 complex and was set to 7 nm [50]. It enters the extension–angle relation $L(\theta) = 2W\sin(\theta/2)$, thereby linking hinge rotation to the axial extension L used in the reduced free-energy landscape. In this way, W provides the geometric conversion between conformational changes in the receptor complex and the mechanical coordinate appearing in the model.

The Morse range parameter d_0 governs the steepness of the binding potential along the separation coordinate and is interpreted here as an effective interaction-range parameter. Since no direct ligand-resolved measurements of d_0 are available for the present systems, we estimated it from representative TCR–pMHC interfacial contact distances extracted from crystallographic structures [88] (see supplementary material). This yielded $d_0 = 0.185$, 0.151 and 0.125 nm for agonists, weak agonists and antagonists, respectively, consistent with Morse range parameters reported for receptor–ligand bonds in force-spectroscopy studies [89].

Taken together, these parameter choices specify the coarse-grained energy landscape for each ligand class used in our work. Among the parameters, only the effective angular stiffness k_θ is inferred phenomenologically from force–lifetime data [6]; the remaining quantities are obtained from affinity, structural, geometric, literature-based or phenomenological estimates, as summarized in table 1. Thus, the subsequent barrier evolution, stationary-point motion and ligand-class-dependent lifetime trends are model outputs conditioned on this phenomenological calibration, rather than fully independent predictions. Together, these parameters define the effective energy.

Downloaded from royalsocietypublishing.org/rsos/article-pdf/doi/10.1098/rsos.252316/6163680/rsos.252316.pdf
by guest
on 02 September 2026

Table 1. Model parameters used in the coarse-grained TCR–pMHC energy-landscape formulation. Representative class-level values used in simulations are shown; full calibration details are provided in the supplementary material. Ag, agonist; Wk, weak agonist; An, antagonist.

parameter	value(s) used	interpretation	source and method
D_0	Ag: 12.0 k_BT; Wk: 9.4 k_BT; An: 7.35 k_BT	maximum binding-well depth	computed from 3D solution affinities (K_D or $\Delta G°$); representative class-level values shown [79–81]
k_θ	Ag: 76.3 pN nm; Wk: 80.9 pN nm; An: 85.3 pN nm	effective angular stiffness of the bound complex	estimated from force-dependent bond-lifetime data using a Boltzmann-like fit; interpreted as an effective coarse-grained parameter [6]
σ	Ag: 0.222 rad; Wk: 0.238 rad; An: 0.482 rad	angular tolerance of $D(\theta)$	agonist-bound structural anchor with free-energy-based scaling; see supplementary material [47,81]
θ_1	Ag: 0.83π; Wk: 0.80π; An: 0.72π	preferred hinge orientation for strongest binding	assigned from the extension–angle relation using $W = 7$ nm; consistent with structural studies [47,50]
d_0	Ag: 0.185 nm; Wk: 0.151 nm; An: 0.125 nm	effective Morse interaction-range parameter	estimated from representative interfacial contact distances; see supplementary material [88]
W	7 nm	effective geometric length scale	fixed shared parameter in $L(\theta) = 2W\sin(\theta/2)$ [50]
θ_0	0.60π	preferred hinge angle of the unloaded state	fixed shared structural parameter [47]

3. Results

3.1. From catch to slip: force-programmed barriers in TCR–pMHC

We examine the impact of external forces on TCR bound with pMHC that has an agonist, weak agonist, and antagonist peptide. An agonist binds to a receptor and activates it, triggering a biological response [90,91]. A weak agonist, as described by [92], also binds but elicits only a partial response, even at full receptor occupancy. An antagonist binds without activation, thus blocking the effects of the agonist [93]. This competitive inhibition was then quantified through dose–response analysis [94].

We examined the influence of an externally applied force oriented along the $(1, 1)$ direction across all ligand classes, focusing on the distinct energetic responses arising from different molecular interactions. Based on the parameter values presented in the previous section, the agonist case displays a non-monotonic dependence of the energy barrier on the applied force. As the force increases, the barrier height rises up to 9 pN, where it reaches a maximum, before decreasing at higher forces. This biphasic pattern is characteristic of a catch–slip bond, in which moderate tensile forces enhance bond stability through barrier strengthening, whereas larger forces promote bond dissociation. This observation is consistent with experimental reports of TCR–pMHC interactions, where force-enhanced stability occurs within an intermediate force range before rupture becomes dominant at high force [18]. A similar, though less pronounced, response is observed in the weak agonist case. Here, the energy barrier increases initially, peaking around 8 pN, followed by a gradual decline at higher forces. This indicates a weaker catch–slip phenotype, consistent with the reduced mechanical reinforcement reported for altered peptide ligands [31]. By contrast, the antagonist case exhibits a monotonic decrease of the energy barrier with increasing force. No intermediate stabilization is observed; instead, the barrier continuously diminishes as the applied force grows. This force-weakening profile reflects a pure slip-bond behaviour, where external force directly facilitates bond dissociation. Such a response mirrors experimental force-spectroscopy observations for non-stimulatory TCR–pMHC interactions, which lack the force-induced stabilization characteristic of agonist complexes [6]. The corresponding force-dependent energy-barrier

Downloaded from royalsocietypublishing.org/rsos/article-pdf/doi/10.1098/rsos.252316/6163680/rsos.252316.pdf
by guest
on 02 September 2026

profiles are shown in figure 4. The detailed numerical values corresponding to these trends are provided in tables 2–4 in appendix A.

In the model, the bond-breaking fold varies across interaction types, occurring at approximately 116 pN for the agonist, 105 pN for the weak agonist and 75 pN for the antagonist. At these critical force levels, the transition state (TS) and the energy minimum (R) merge at the BBP, so that the reduced landscape no longer contains a distinct bound minimum and adjacent saddle. These values should therefore be interpreted as model-internal fold points of the simplified energy landscape, rather than as direct physiological rupture-force predictions. This phenomenon underscores the interplay between force magnitude and molecular stability, providing insight into the mechanistic principles governing catch–slip bond behaviour.

The PES diagrams (figure 5) illustrate how the TCR extension (L) and the distance to the ligand (d) affect the stability of the TCR–pMHC bond under varying force conditions. Each contour plot represents the equipotential lines of the potential energy function in the (L, d) coordinate space, where the two length coordinates (L and d, in nm) describe the movement of the ligand. To help visualize this more clearly, we also include a representative three-dimensional PES in figure 6, where the barrier between the bound minimum and SP is seen more directly.

The reactant (R) corresponds to the global minimum of the PES, representing the bound state of the ligand–receptor interaction. The TS is a SP1 of index one, signifying the energy peak that must be overcome for bond dissociation. The BBP marks the moment when an applied force causes the former minimum (R) and the SP1 to coincide, resulting in bond rupture. The Det($\mathbf{H}$) = 0 lines, shown in green, indicate critical points where the determinant of the Hessian matrix vanishes, signifying structural transitions in the energy landscape that impact molecular stability and interactions.

The bold curve is the NT. On it, the minimum and SP1 move. After the minimum, because of the direction, $(1, 1)$, the NT ascends strongly into the PES mountains for higher L values. This also causes an increasing barrier height, thus a catch-bond behaviour. We plotted the PES for different force values, considering the cases of an agonist, weak agonist and antagonist.

For the agonist in the forceless limit ($F = 0$), the PES is represented by thin equipotential lines, with R as the global minimum, indicating the bound state. The TS, corresponding to the dissociation limit, lies far beyond the displayed scale. The thick NT along the (1,1) direction represents a slip–catch–slip bond transition. The Det($\mathbf{H}$) = 0 lines, shown in green, highlight critical points in the PES where the determinant of the Hessian matrix vanishes, signalling structural transitions in the energy landscape. For the case of $F = 10$ pN, we observe a single minimum (R) and a single SP. Notably, the solid NT has a TP, which may serve as an indicator of a catch-bond mechanism, suggesting force-enhanced binding stability. Finally, at a high force of $F = 116$ pN, the former TS and the former minimum (R) merge to form a shoulder, indicating the disappearance of the energy barrier.

For the weak agonist, in a similar way for the case of $F = 10$ pN, we observe a single minimum (R) and a single SP. Notably, the solid NT has a TP, which may serve as an indicator of a catch-bond mechanism, suggesting force-enhanced binding stability. At a high force of $F = 105$ pN, the former TS and the former minimum (R) merge to form a shoulder, indicating the disappearance of the energy barrier.

In conclusion, forces applied along the (1, 1) direction reveal distinct, peptide-class-specific mechanical responses. Agonists exhibit a characteristic catch–slip profile, in which the energy barrier increases up to approximately 9 pN before declining at higher loads. Weak agonists show a similar but attenuated peak near 8 pN, whereas antagonists behave as pure slip bonds, displaying a monotonic barrier decay. Bond-rupture events occur when the bound minimum and transition state merge, at roughly 116 pN for agonists, 105 pN for weak agonists and 75 pN for antagonists (for antagonists see figure 10 in appendix B). Analysis of the PES and NTs—organized by lines where Det($\mathbf{H}$) = 0—links these outcomes to the underlying force-reshaped energy landscapes in (L, d) space. Moderate mechanical loads can transiently stabilize agonist binding, whereas larger forces universally promote bond dissociation across all classes.

3.2. Force-dependent bond lifetimes

The mean bond lifetime, particularly in the context of adhesion, unbinding and bond stability, is influenced by an energy barrier that must be overcome for bond dissociation. Theoretical models such as the Arrhenius kinetics and Kramers' rate theory offer a framework to quantify bond dissociation under thermal fluctuations and external forces [95,96]. In the overdamped (Smoluchowski) regime, the lifetime

Downloaded from royalsocietypublishing.org/rsos/article-pdf/doi/10.1098/rsos.252316/6163680/rsos.252316.pdf
by guest
on 02 September 2026

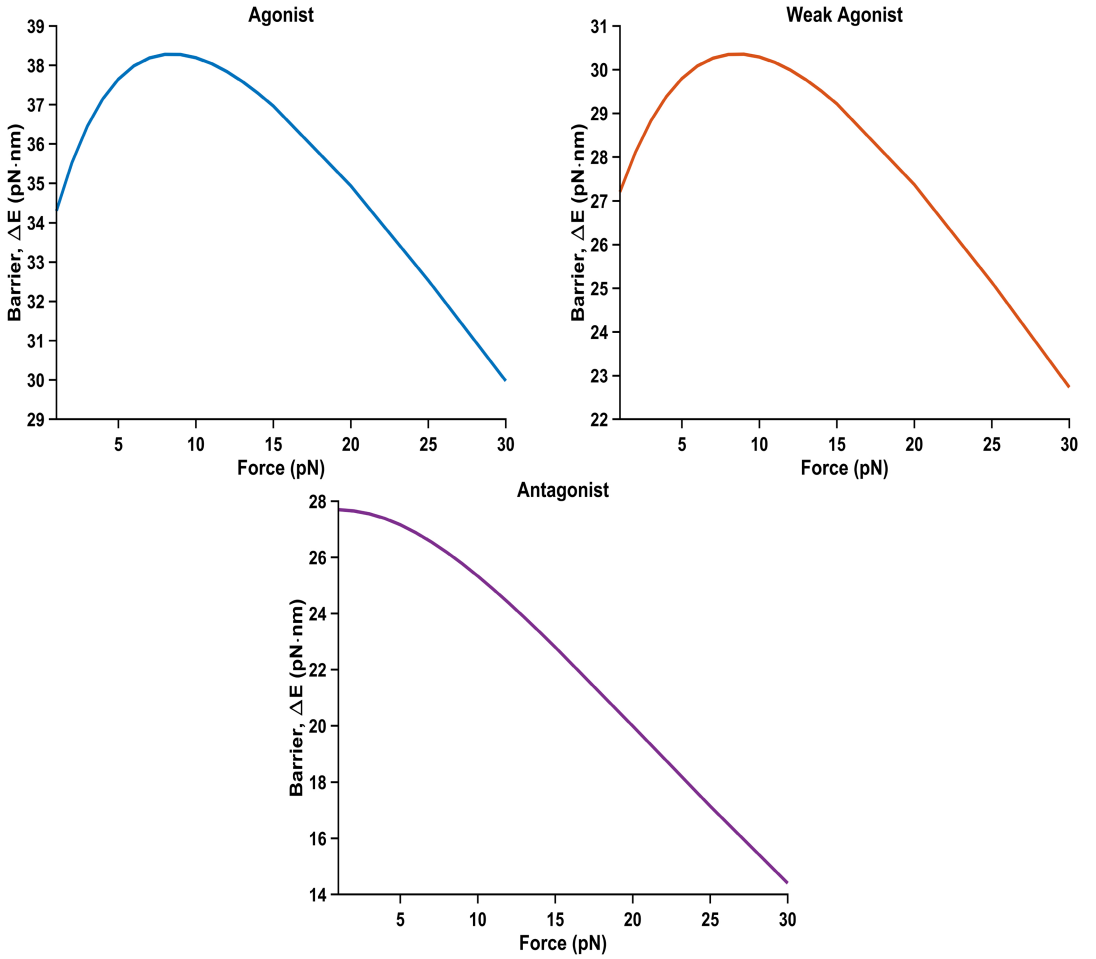


Figure 4. Force-dependent barrier $\Delta E(F) = V_f(\mathbf{x}_s; F) - V_f(\mathbf{x}_m; F)$ for agonist, weak agonist and antagonist interactions.

of the bond, τ, is commonly estimated using an Arrhenius-type equation:

$$\tau = \tau_0 e^{\Delta E/k_B T}, \tag{3.1}$$

where ΔE represents the energy barrier, k_B is the Boltzmann constant, T is the absolute temperature and τ_0 is a prefactor that accounts for the attempt frequency of escape from the potential well [97].

This energy barrier ΔE can also be represented by $\Delta E = V_f(\mathbf{x}_s) - V_f(\mathbf{x}_m)$, where the vectors $\mathbf{x}_m = (L_m, d_m)$ and $\mathbf{x}_s = (L_s, d_s)$ denote, respectively, the positions in configuration space of the local minimum (the bound state) and SP (the transition state) of V_f. At human body temperature, the thermal energy scale is given by $k_B T \approx 4.28$ pN nm, which provides a natural unit for comparing energy barriers in molecular interactions.

The prefactor τ_0 for the escape rate in Langer's [98] metastable decay theory is given by

$$\tau_0 = \frac{2\pi}{\lambda_+} \cdot \sqrt{\frac{|\det \mathbf{H}^\ddagger|}{\det \mathbf{H}_A}}.$$

Here, λ_+ is given by $\lambda_+ = -\beta D h_{uu}$, where β is the inverse thermal energy, defined as $\beta = 1/k_B T$, with k_B being the Boltzmann constant and T the temperature in kelvin. The parameter D denotes the (isotropic) diffusion coefficient (units nm^2 s^{-1}; related to friction by the Einstein relation $D = k_B T/\zeta$), which accounts for frictional effects in Kramers' theory. The term $\det \mathbf{H}_A$ denotes the determinant of the Hessian matrix at the local minimum, while $\det \mathbf{H}^\ddagger$ represents the determinant of the Hessian matrix at the SP (the absolute value is taken because an index-1 saddle has $\det \mathbf{H}^\ddagger < 0$). Additionally, $h_{uu} = \boldsymbol{e}_u^\top \mathbf{H}^\ddagger \boldsymbol{e}_u < 0$ is the unstable curvature (negative eigenvalue) of the saddle Hessian along the unit unstable direction $\boldsymbol{e}_u$. With V_f ex-

Downloaded from royalsocietypublishing.org/rsos/article-pdf/doi/10.1098/rsos.252316/6163680/rsos.252316.pdf
by guest
on 02 September 2026

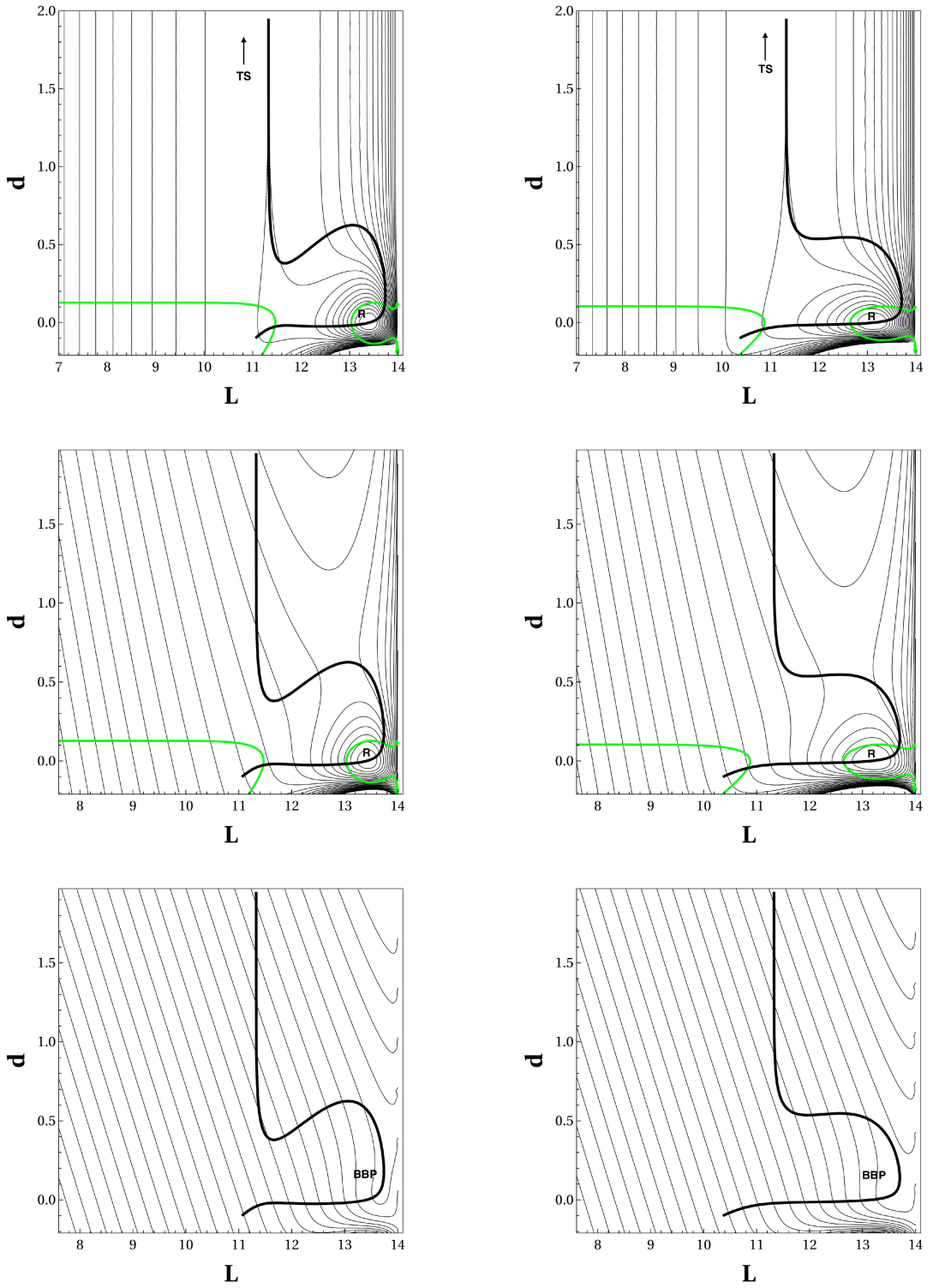


Figure 5. 2D PES for TCR–pMHC interactions under different forces. The left column corresponds to the agonist, and the right column to the weak agonist. From top to bottom: $F = 0$, $F = 10$, and high-force conditions ($f = 116$ for agonist and $F = 105$ for weak agonist). Equipotential contours represent energy landscapes under each condition; R denotes the bound-state minimum, TS the adjacent SP and BBP the bond-breaking point where the minimum and saddle coalesce.

Downloaded from royalsocietypublishing.org/rsos/article-pdf/doi/10.1098/rsos.252316/6163680/rsos.252316.pdf
by guest
on 02 September 2026

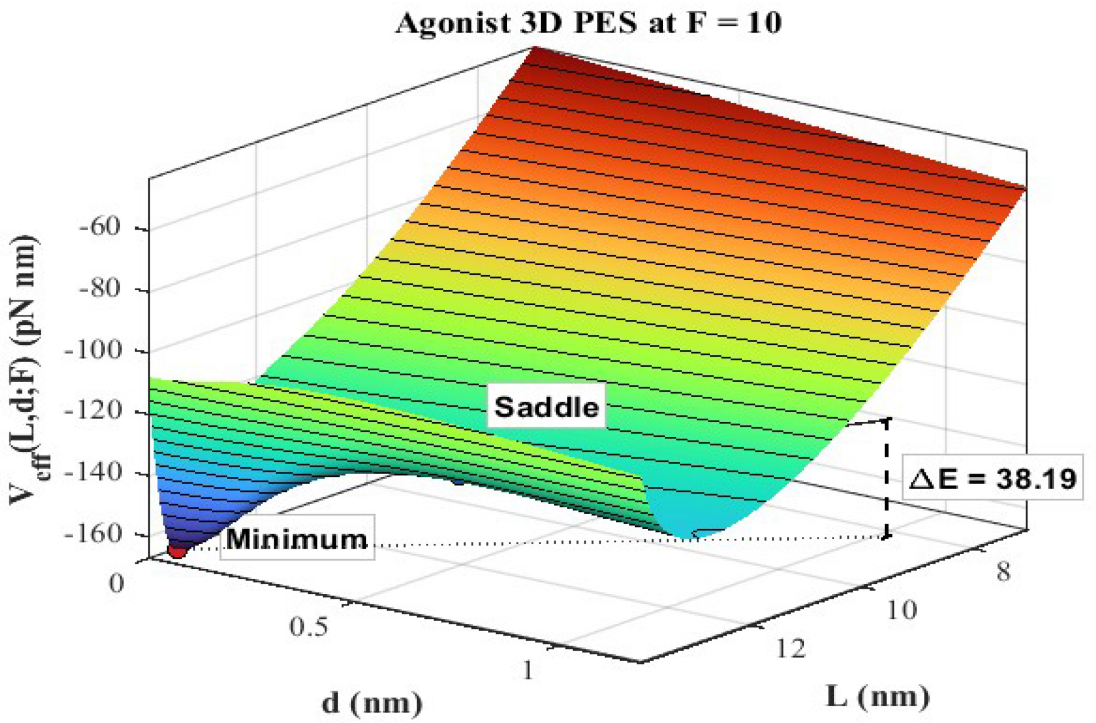


Figure 6. Representative three-dimensional effective PES $V_{\text{eff}}(L, d; F)$ for the agonist at $F = 10$, showing the bound minimum, SP and barrier height ΔE.

pressed in pN nm and the coordinates L and d expressed in nm, the Hessian entries have units of pN nm^{-1}, and the Hessian determinants in two dimensions have units of (pN nm^{-1})^2. Hence, the determinant ratio in the Kramers–Langer prefactor is dimensionless. Since β has units (pN nm)$^{-1}$, D has units nm^2 s^{-1} and h_{uu} has units pN nm^{-1}, the quantity λ_+ has units s^{-1}. Therefore, the prefactor τ_0, and consequently the lifetime τ, are expressed in seconds.

The bond lifetime (τ) as a function of applied force was analysed for three ligand types: agonist, weak agonist and antagonist. Each ligand exhibited a distinct bond lifetime in response to increasing force (see figure 7). Analysis of the computed lifetimes (τ) as a function of applied force reveals distinct mechanochemical behaviours across the three peptide classes. In the agonist case, bond lifetime increases from 0.83 seconds at 1 pN to a maximum of approximately 1.29 seconds at 9 pN, beyond which it gradually declines to 0.24 seconds by 30 pN. This biphasic trend indicates a catch–slip transition, where moderate tensile forces stabilize the complex through an increased energy barrier, while higher forces promote bond rupture. In the weak-agonist case, the bond lifetime exhibits a small initial dip, decreasing from 0.22 seconds at 1 pN to 0.20 seconds at 2 pN, which arises from competition between the force-dependent prefactor and the barrier term. The lifetime then increases modestly to a shallow maximum of approximately 0.24 seconds at 8 pN, before decreasing again to about 0.04 seconds at 30 pN.

This subtle peak suggests a weak or transient catch-bond behaviour, with limited mechanical reinforcement compared with the full agonist. By contrast, the antagonist exhibits a strictly monotonic decay in lifetime with increasing force, characteristic of a pure slip bond, where external load directly facilitates dissociation rather than stabilization.

Overall, only agonists display a pronounced catch–slip profile, consistent with their ability to enhance bond stability under physiological force ranges and thereby promote TCR activation. Weak agonists show marginal or inconsistent stabilization, while antagonists destabilize under load, reflecting their inhibitory role in T-cell signalling.

3.3. Sensitivity analysis

To assess the local sensitivity of the force-dependent barrier and lifetime predictions around the fitted parameter values, we performed a bounded Latin hypercube sampling–partial rank correlation coefficient (LHS–PRCC) [99,100] analysis around the agonist, weak agonist and antagonist baselines.

Downloaded from royalsocietypublishing.org/rsos/article-pdf/doi/10.1098/rsos.252316/6163680/rsos.252316.pdf
by guest
on 02 September 2026

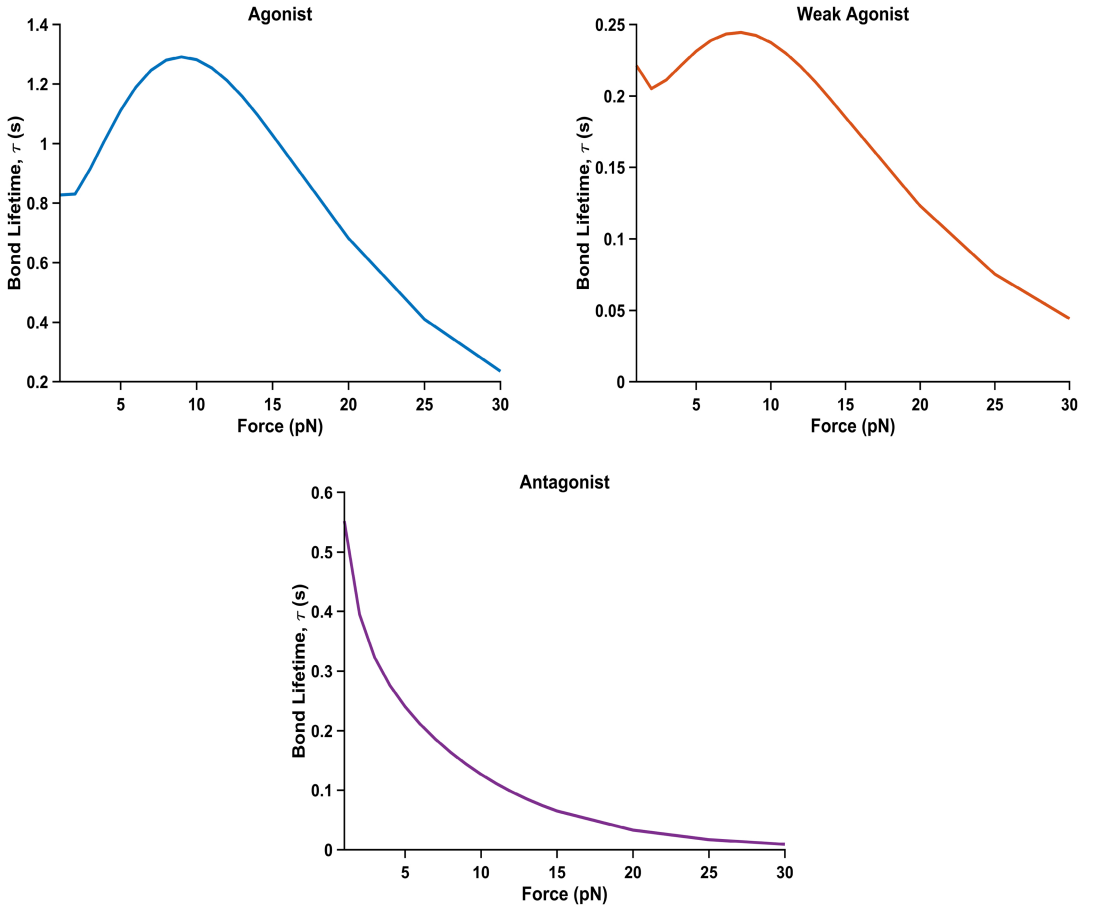


Figure 7. Bond lifetime (τ) as a function of force (F) for agonist, weak agonist and antagonist interactions. The agonist shows catch–slip behaviour, with lifetime peaking around 8–9 pN. The weak agonist exhibits mild or transient stabilization, indicating limited mechanical reinforcement, whereas the antagonist exhibits a monotonic decrease consistent with pure slip-bond behaviour.

For each ligand class, the fitted parameters k_θ, D_0, θ_1, σ and d_0 were perturbed independently within ±5% of their class-specific baseline values, while the shared structural parameters W and θ_0 were held fixed. For each sampled parameter set, we computed the force-dependent barrier and bond lifetime over the prescribed force range and summarized the resulting lifetime curve using four descriptors. The peak lifetime was defined as the maximum lifetime attained along the force curve, and the force at peak lifetime as the force value at which this maximum occurred. The catch-phase amplitude was defined as the increase from the initial valid lifetime to the peak, thereby quantifying the strength of the catch phase, whereas the slip-phase drop was defined as the decrease from the peak to the final valid lifetime, thereby quantifying the strength of the subsequent slip phase. Together, these descriptors capture the scale, location and overall non-monotonic structure of the lifetime response.

Parameter influence was quantified using PRCC, such that positive values indicate that increasing a parameter tends to increase the corresponding descriptor, whereas negative values indicate the opposite trend. The resulting sensitivity analysis revealed a clear separation of parameter roles across ligand classes (figure 8). In all three regimes, D_0 was the dominant positive determinant of peak lifetime, indicating that it primarily controls the overall lifetime scale. By contrast, θ_1 was the dominant determinant of the force-dependent shape of the response, strongly influencing both the force at peak lifetime and the rise-and-fall structure associated with catch–slip behaviour. Thus, the analysis supports a mechanistic distinction in which D_0 mainly sets the magnitude of the barrier/lifetime response, whereas θ_1 mainly governs how that response is reorganized under force.

The weak agonist regime preserved the same primary sensitivity hierarchy as the agonist case, but exhibited stronger secondary contributions from d_0, σ and k_θ, consistent with a more distributed and less robust force–response structure. In the antagonist regime, D_0 still governed the overall lifetime scale, but the sampled lifetime curves did not exhibit a consistently defined interior maximum. As a result, descriptors that rely on a robust catch phase, such as the force at peak lifetime and the catch-phase am-

Downloaded from royalsocietypublishing.org/rsos/article-pdf/doi/10.1098/rsos.252316/6163680/rsos.252316.pdf
by guest
on 02 September 2026

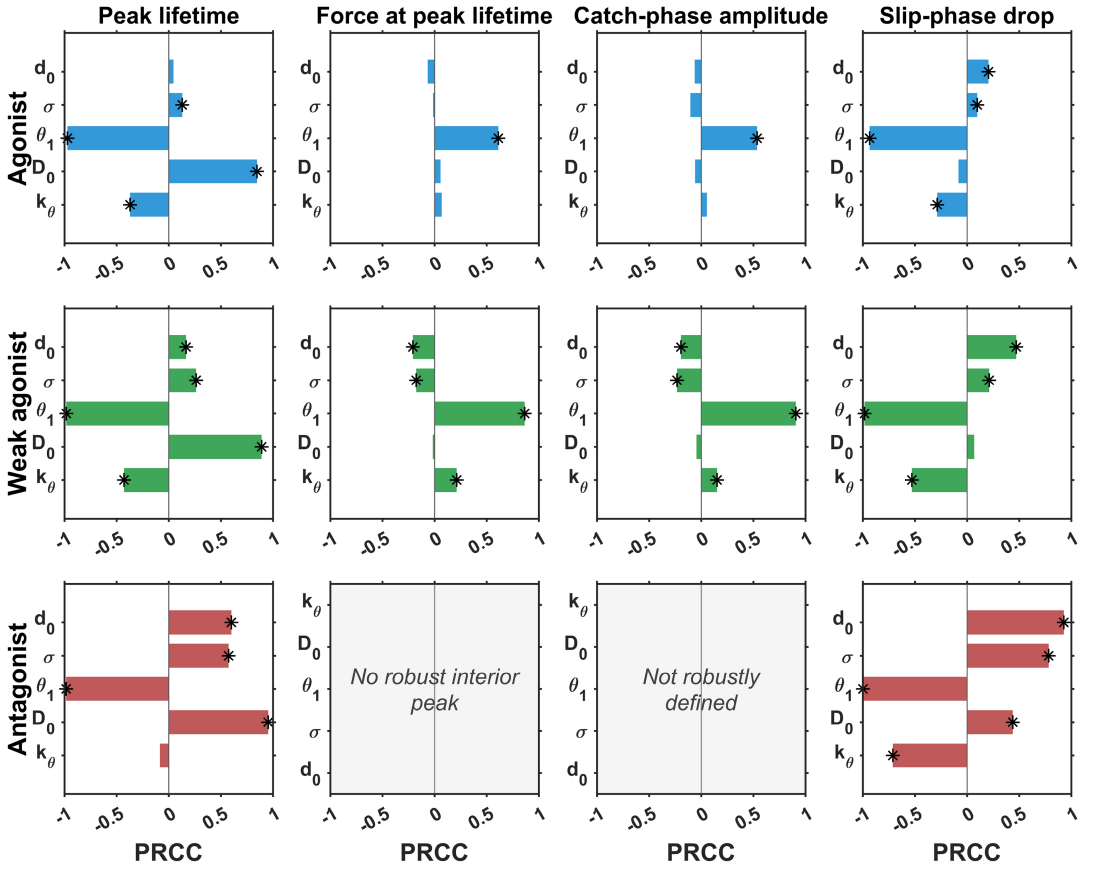


Figure 8. Sensitivity analysis of peak lifetime and catch-slip descriptors across ligand classes.

plitude, were not stably defined across the sampled neighbourhood. Taken together, these results show that the principal conclusions of the model are not artefacts of a single fitted parameter set, but remain structurally stable under bounded perturbations around each ligand-class baseline. In particular, the dominant roles of D_0 and θ_1 remain qualitatively preserved, reinforcing the interpretation that overall binding strength and force-dependent geometric control make distinct contributions to the emergence of catch–slip behaviour. This strengthens confidence that the model captures a robust mechanochemical structure rather than a calibration-specific effect.

For completeness, the full force-resolved PRCC heatmaps for bond lifetime, barrier height and prefactor, together with the barrier-side summary sensitivities, are provided in the supplementary material.

4. Discussion

Within a mechanochemical framework, we combined NT analysis of the loaded PES V_f (equation (2.7)) with Arrhenius–Kramers theory to relate force-driven changes in the energy landscape to bond lifetime. This approach allowed us to track how minima and saddles migrate under load, identify the BBP at which they coalesce, establish an existence–stability threshold for steady states and connect barrier reshaping to experimentally observed bond-lifetime patterns across peptide classes. In particular, the model reproduces catch–slip behaviour for agonists and weak agonists, and slip behaviour for antagonists, within a unified force-coupled landscape.

A central mathematical result is the emergence of a model-internal fold threshold, $F_c = D_0/(2d_0)$, which separates regimes with and without steady states in the reduced energy landscape. For $F > F_c$, no steady states exist, whereas for $0 \le F \le F_c$, there are at most two, typically corresponding to a minimum–saddle pair. A single solution arises only in degenerate parameter choices. When steady states exist, they are obtained by solving $J(\theta) = 0$ on the admissible set Θ, followed by reconstruction of u, d and L. Local stability is possible only on the near branch $u > 1/2$ with $\det H > 0$; at the fold $u = 1/2$, the minimum and saddle coalesce, marking the BBP and the loss of stability. Thus, F_c represents an existence threshold

Downloaded from royalsocietypublishing.org/rsos/article-pdf/doi/10.1098/rsos.252316/6163680/rsos.252316.pdf
by guest
on 02 September 2026

for bound stationary configurations in the simplified landscape, not a direct physiological rupture-force prediction. The biologically relevant catch–slip modulation occurs below this fold, where force reshapes the barrier and lifetime before the bound state is lost.

To parametrize the model, we combined affinity-derived energetic scales, structural and geometric inputs, literature-based estimates and calibration of k_θ against force-dependent lifetime data. Binding strength D_0 was derived from reported K_D values through the standard-state relation $D_0 = -k_B T \ln(K_D/1\ \mathrm{M})$, the angular width σ was inferred from the FWHM of hinge-angle distributions, and the angular stiffness k_θ was estimated by fitting force-dependent bond lifetimes using an Arrhenius–Kramers form. The interaction range d_0 was chosen from class-specific literature estimates, while the geometric scale W and the $\theta \leftrightarrow L$ relation were fixed from cryo-EM-informed structure. These calibrated inputs populate the Gaussian angular binding term $D(\theta)$ and the Morse distance term $B(d, \theta)$ in the energy landscape. With these inputs, the model yields class-specific mechanical phenotypes: agonist and weak-agonist peptides exhibit catch–slip behaviour in their barriers and lifetimes, whereas antagonists display monotonic slip behaviour.

The novelty of the present work lies in formulating and analysing a two-dimensional TCR–pMHC-specific mechanochemical energy landscape, rather than in proposing the general idea that energy landscapes can generate catch–slip kinetics. Our approach combines a minimal, data-anchored energy landscape with NT analysis to derive interpretable criteria for existence, stability and bond breaking. Unlike simulation-heavy pipelines, the framework yields compact analytical conditions, such as the threshold $F_c = D_0/(2d_0)$ and the stability condition $u > 1/2$, while still linking barrier reshaping directly to bond lifetime. By treating receptor extension and binding-site separation as coupled coordinates, the model provides a TCR–pMHC-specific framework for tracking force-dependent minima, saddles, BBPs, barriers and lifetimes. This balance between tractability and mechanistic interpretation makes the model useful not only for reproducing ligand-class-specific trends but also for clarifying how force reorganizes the underlying energy landscape. In this sense, the framework complements earlier perspectives on TCR sensitivity and selectivity. For example, Klotzsch & Schütz proposed that force may enhance ligand discrimination through force-dependent unbinding dynamics [14], whereas kinetic proofreading explains selectivity through sequential biochemical filtering after receptor engagement [8]. Our model isolates one specific contribution within this broader picture, namely how force-dependent barrier reshaping can generate ligand-class-dependent bond-lifetime behaviour. These ligand-class-specific behaviours therefore arise from the combination of peptide-dependent allosteric landscape structure and force-induced barrier reshaping, rather than from force acting on identical unloaded landscapes.

Our parameter choices provide a practical first calibration, but naturally carry uncertainty for barrier and lifetime estimates. Since k_θ is calibrated from force–lifetime data, the lifetime curves are best viewed as phenomenological consistency checks of the proposed energy landscape rather than as fully independent predictions. Importantly, the bounded sensitivity analysis showed that the principal qualitative conclusions of the model remain stable under local perturbations around each ligand-class baseline. In particular, the dominant role of D_0 in setting the overall lifetime scale and of θ_1 in shaping the force-dependent catch–slip structure was qualitatively preserved across the sampled parameter neighbourhoods. This supports the interpretation that the mechanochemical organization inferred by the model reflects a robust local structure rather than a calibration-specific artefact.

The present model is therefore best viewed as a framework for TCR–pMHC barrier reshaping and bond lifetime, not as a complete model of T-cell activation or antigen specificity. Productive TCR triggering may require bond lifetimes within an appropriate mechanical range, together with CD8/coreceptor engagement and downstream signalling context, which are not explicitly represented here [101].

Because D_0, k_θ and σ enter the landscape in different ways, the model separates binding strength from angular compliance. Increasing D_0 deepens the binding well, whereas k_θ and σ determine how readily the complex can reorganize under load. Very stable binding may therefore coexist with limited angular rearrangement, which could restrict CD8 cooperation and downstream triggering [101].

To make the scope of the framework explicit, the model includes TCR–pMHC barrier reshaping, hinge elasticity, angle-dependent binding strength, force-dependent movement of minima and saddles, BBPs and Kramers–Langer lifetime estimation. It does not explicitly include CD8 coreceptor engagement, membrane mechanics, cytoskeletal loading history, downstream signalling or peptide-specific conformational pathways. These excluded processes may be important for productive TCR triggering, but they lie outside the present minimal energy-landscape formulation.

At the same time, the model is deliberately minimal in order to keep the physics transparent. The present formulation assumes a Gaussian angular approximation and constant loading, and it does not yet explicitly include membrane mechanics, viscoelastic response or peptide-specific shifts in θ_1. These

Downloaded from royalsocietypublishing.org/rsos/article-pdf/doi/10.1098/rsos.252316/6163680/rsos.252316.pdf
by guest
on 02 September 2026

simplifications make the model analytically interpretable, but they also limit its ability to capture the full complexity of cellular force transmission. Improved peptide- and system-specific measurements of angular distributions, effective stiffness, interaction range and force history would help refine the calibration and increase predictive power. With such data, the framework could be extended to circular angle statistics, time-dependent loading and membrane-coupled effects to better reflect physiological conditions.

Overall, our results support a mechanochemical interpretation of force-dependent TCR–pMHC bond regulation in which force does not merely accelerate bond rupture but can reorganize the energy landscape in a ligand-dependent manner. By linking force, barrier structure and bond lifetime within a compact analytical framework, the model provides a clear and testable basis for understanding how EC load may contribute to early TCR–pMHC recognition processes.

Ethics. This work did not require ethical approval from a human subject or animal welfare committee.

Data accessibility. All data, numerical results and computational code needed to reproduce the findings of this study are available at GitHub: http://github.com/Ybali-del/TCR-mechanochemical-model.

Declaration of AI use. We have not used AI-assisted technologies in creating this article.

Authors' contributions. Y.B.B.: conceptualization, data curation, formal analysis, investigation, methodology, resources, validation, visualization, writing—original draft, writing—review and editing; A.R.: investigation, project administration, supervision, validation, writing—review and editing; W.Q.: formal analysis, investigation, methodology, project administration, supervision, validation, visualization, writing—review and editing.

All authors gave final approval for publication and agreed to be held accountable for the work performed therein.

Conflict of interest declaration. We declare we have no competing interests.

Funding. No funding has been received for this article.

Appendix A. Summary of stationary points and barrier heights for agonist, weak agonist and antagonist ligands

This appendix provides the numerical results corresponding to the stationary points and transition-state energies of the effective potential V_{eff} governing the TCR–pMHC interaction. For each ligand class—agonist, weak agonist and antagonist—the equilibrium minima and SPs were computed along the NT reaction coordinate $\frac{1}{\sqrt{2}}(1,1)$. Tables 2–4 (agonist, weak agonist and antagonist, respectively) list the values of the extension L, ligand separation d and the corresponding potential energies (in pN nm), from which the barrier heights were derived. These data form the quantitative basis for the force-dependent bond lifetimes and transition analyses discussed in the main text.

Table 2. Stationary points of the effective potential V_{eff} for the TCR–pMHC interaction, obtained along the NT direction $\frac{1}{\sqrt{2}}(1,1)$. Energies are given in pN nm.

F	Min (L, d) [nm]	V_{Min} [pN]	SP (L, d) [nm]	V_{SP} [pN]	barrier
1	(13.4101, 0.0003)	−46.2752	(11.6634, 0.3804)	−11.9705	34.3047
2	(13.4139, 0.0007)	−59.6878	(11.9297, 0.4167)	−24.1668	35.5210
3	(13.4177, 0.0010)	−73.1045	(12.1439, 0.4676)	−36.6497	36.4548
4	(13.4214, 0.0014)	−86.5253	(12.3204, 0.5114)	−49.3748	37.1505
5	(13.4251, 0.0017)	−99.9501	(12.4680, 0.5459)	−62.3005	37.6496

(*Continued*.)

Downloaded from royalsocietypublishing.org/rsos/article-pdf/doi/10.1098/rsos.252316/6163680/rsos.252316.pdf
by guest
on 02 September 2026

Table 2. (*Continued.*)

F	**Min** (L, d) **[nm]**	V_{Min} **[pN]**	**SP** (L, d) **[nm]**	V_{SP} **[pN]**	**barrier**
6	(13.4287, 0.0021)	−113.3789	(12.5930, 0.5721)	−75.3924	37.9865
7	(13.4323, 0.0024)	−126.8116	(12.6998, 0.5915)	−88.6225	38.1891
8	(13.4358, 0.0028)	−140.2483	(12.7919, 0.6054)	−101.9684	38.2799
9	(13.4393, 0.0031)	−153.6887	(12.8720, 0.6150)	−115.4082	38.2805
10	(13.4427, 0.0035)	−167.1330	(12.9421, 0.6210)	−128.9378	38.1952
11	(13.4461, 0.0038)	−180.5811	(13.0039, 0.6243)	−142.5343	38.0468
12	(13.4495, 0.0042)	−194.0328	(13.0586, 0.6255)	−156.1912	37.8416
13	(13.4528, 0.0045)	−207.4883	(13.1075, 0.6249)	−169.9000	37.5883
14	(13.4560, 0.0049)	−220.9474	(13.1512, 0.6229)	−183.6537	37.2937
15	(13.4593, 0.0052)	−234.4101	(13.1906, 0.6199)	−197.4464	36.9637
20	(13.4750, 0.0071)	−301.7768	(13.3396, 0.5947)	−266.8417	34.9351
25	(13.4899, 0.0090)	−369.2294	(13.4373, 0.5624)	−336.6935	32.5359
30	(13.5042, 0.0109)	−436.7647	(13.5056, 0.5291)	−406.7888	29.9759

Table 3. Stationary points of the PES V_{eff} for the TCR–pMHC interaction by equation (2.1), along the NT direction $\frac{1}{\sqrt{2}}(1, 1)$. Energies are in pN nm.

F	**Min** (L, d) **[nm]**	V_{Min} **[pN]**	**SP** (L, d) **[nm]**	V_{SP} **[pN]**	**barrier**
1	(13.1523, 0.0003)	−39.3487	(11.5877, 0.5744)	−12.1439	27.2048
2	(13.1613, 0.0006)	−52.5060	(11.8089, 0.5407)	−24.3981	28.1079
3	(13.1699, 0.0009)	−65.6723	(11.9974, 0.5368)	−36.8414	28.8309
4	(13.1784, 0.0012)	−78.8476	(12.1592, 0.5395)	−49.4596	29.3880
5	(13.1867, 0.0015)	−92.0315	(12.2991, 0.5431)	−62.2318	29.7997
6	(13.1948, 0.0018)	−105.2239	(12.4210, 0.5459)	−75.1378	30.0861
7	(13.2027, 0.0021)	−118.4245	(12.5278, 0.5473)	−88.1601	30.2644
8	(13.2105, 0.0024)	−131.6334	(12.6220, 0.5473)	−101.2834	30.3500
9	(13.2181, 0.0027)	−144.8502	(12.7056, 0.5460)	−114.4948	30.3554
10	(13.2255, 0.0029)	−158.0748	(12.7801, 0.5435)	−127.7832	30.2916
11	(13.2328, 0.0032)	−171.3071	(12.8468, 0.5402)	−141.1391	30.1680

(*Continued.*)

Downloaded from royalsocietypublishing.org/rsos/article-pdf/doi/10.1098/rsos.252316/6163680/rsos.252316.pdf
by guest
on 02 September 2026

Table 3. (*Continued.*)

F	**Min** (L, d) **[nm]**	V_{Min} **[pN]**	**SP** (L, d) **[nm]**	V_{SP} **[pN]**	**barrier**
12	(13.2400, 0.0035)	−184.5469	(12.9068, 0.5360)	−154.5546	29.9923
13	(13.2471, 0.0038)	−197.7941	(12.9610, 0.5312)	−168.0226	29.7715
14	(13.2540, 0.0042)	−211.0486	(13.0101, 0.5259)	−181.5371	29.5115
15	(13.2608, 0.0045)	−224.3104	(13.0549, 0.5201)	−195.0930	29.2174
20	(13.2933, 0.0060)	−290.7229	(13.2283, 0.4881)	−263.3533	27.3696
25	(13.3237, 0.0076)	−357.3004	(13.3458, 0.4543)	−332.1620	25.1384
30	(13.3523, 0.0093)	−424.0334	(13.4296, 0.4215)	−401.3006	22.7328

Table 4. Stationary points on the PES V_{eff} of the TCR–pMHC complex (equation (2.1)), along the NT direction $\frac{1}{\sqrt{2}}(1, 1)$. Energies are given in pN nm.

F	**Min** (L, d) **[nm]**	V_{Min} **[pN]**	**SP** (L, d) **[nm]**	V_{SP} **[pN]**	**barrier**
1	(12.2427, 0.0003)	−39.9972	(11.5232, 0.7483)	−12.2956	27.7016
2	(12.2963, 0.0005)	−52.2673	(11.6993, 0.6688)	−24.6122	27.6551
3	(12.3468, 0.0008)	−64.5897	(11.8573, 0.6238)	−37.0367	27.5530
4	(12.3948, 0.0010)	−76.9616	(11.9993, 0.5922)	−49.5735	27.3881
5	(12.4403, 0.0013)	−89.3805	(12.1274, 0.5677)	−62.2174	27.1631
6	(12.4838, 0.0015)	−101.8441	(12.2431, 0.5474)	−74.9609	26.8832
7	(12.5253, 0.0018)	−114.3505	(12.3480, 0.5299)	−87.7958	26.5547
8	(12.5650, 0.0020)	−126.8976	(12.4434, 0.5143)	−100.7142	26.1834
9	(12.6031, 0.0023)	−139.4840	(12.5303, 0.5002)	−113.7088	25.7752
10	(12.6397, 0.0026)	−152.1079	(12.6097, 0.4872)	−126.7730	25.3349
11	(12.6749, 0.0028)	−164.7680	(12.6824, 0.4751)	−139.9007	24.8673
12	(12.7088, 0.0031)	−177.4629	(12.7491, 0.4638)	−153.0863	24.3766
13	(12.7415, 0.0034)	−190.1914	(12.8105, 0.4531)	−166.3249	23.8665
14	(12.7731, 0.0036)	−202.9523	(12.8671, 0.4428)	−179.6119	23.3404
15	(12.8037, 0.0039)	−215.7446	(12.9194, 0.4331)	−192.9434	22.8012
20	(12.9426, 0.0054)	−280.1424	(13.1295, 0.3897)	−260.1512	19.9912
25	(13.0623, 0.0071)	−345.1928	(13.2786, 0.3528)	−328.0457	17.1471
30	(13.1668, 0.0089)	−410.8113	(13.3883, 0.3205)	−396.4078	14.4035

Downloaded from royalsocietypublishing.org/rsos/article-pdf/doi/10.1098/rsos.252316/6163680/rsos.252316.pdf
by guest
on 02 September 2026

Appendix B. Supplementary figures

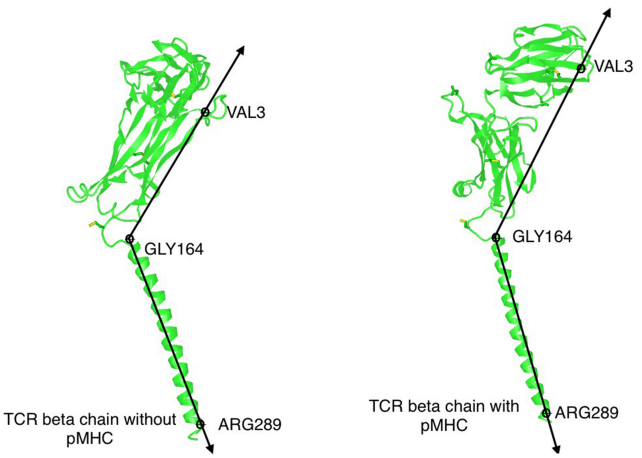


Figure 9. Visualization of the atoms used to calculate the tilt angle, specifically TCRβ residues VAL_3, GLY_{164} and ARG_{289}. The left panel shows the TCRβ chain in its unbound state, while the right panel displays the TCRβ chain in complex with pMHC, highlighting a shift in the tilt angle from 104.99° to 147.56° upon ligand binding.

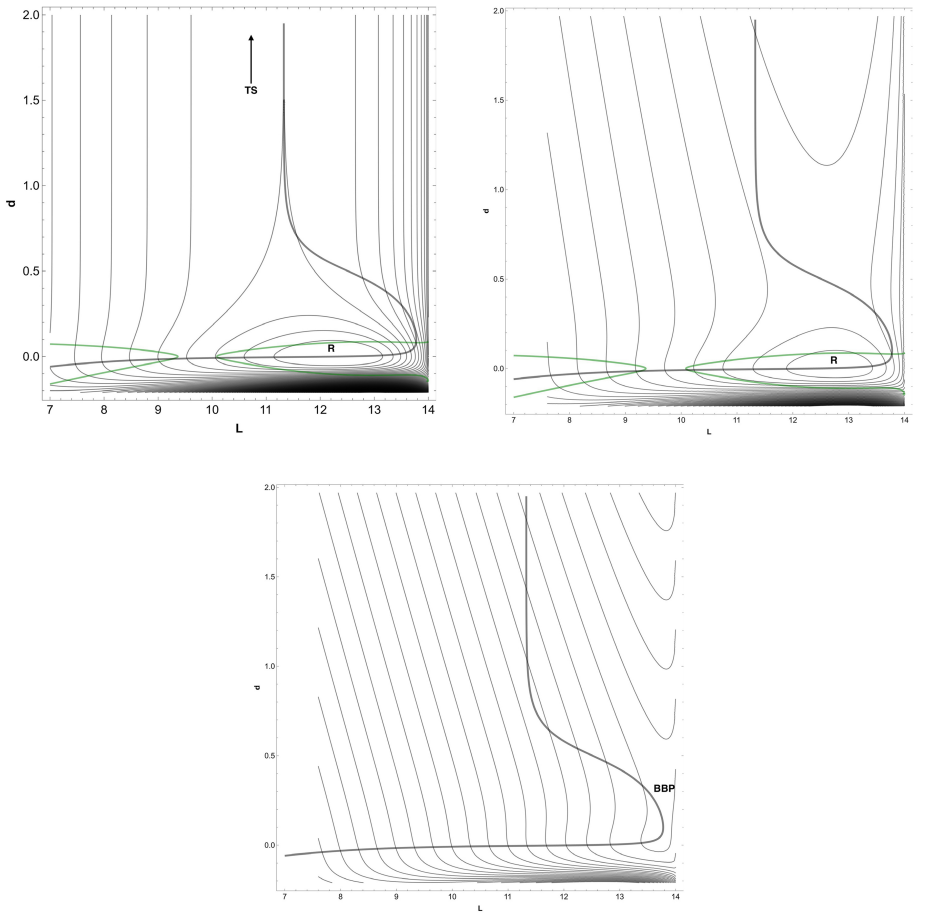


Figure 10. 2D PES for TCR–antagonist–pMHC interaction under high force ($f = 75$), showing deformation of the energy landscape with applied load.

Downloaded from royalsocietypublishing.org/rsos/article-pdf/doi/10.1098/rsos.252316/6163680/rsos.252316.pdf
by guest
on 02 September 2026

Appendix C. Mathematical analysis

Theorem C.1 (Existence and multiplicity of steady states). *Assume $W > 0$, $d_0 > 0$, $D_0 > 0$, $\sigma > 0$, $k_\theta > 0$ and $F \geq 0$. Let*

$$\alpha := \frac{Fd_0}{2}, \quad D(\theta) = D_0\, \mathrm{e}^{-(\theta-\theta_1)^2/(2\sigma^2)}, \quad C(\theta) = \frac{\alpha}{D(\theta)}, \quad B(\theta) = \frac{\theta-\theta_1}{\sigma^2}\, D(\theta),$$

$$A(\theta) = k_\theta(\theta-\theta_0) + \frac{\alpha}{\sigma^2}(\theta-\theta_1), \qquad R(\theta) = FW\cos\Big(\frac{\theta}{2}\Big), \qquad J(\theta) = (R-A)B - (R-A)^2 - C(\theta)B^2,$$

and define the admissible set $\Theta := \{\theta \in [0,\pi] : D(\theta) \geq 2Fd_0\}$ (nonempty iff $D_0 \geq 2Fd_0$). Then:

- *If $D_0 < 2Fd_0$ (equivalently, $F > D_0/(2d_0)$), then $\Theta = \varnothing$ and there are no steady states.*
- *If $D_0 \geq 2Fd_0$, a pair (L^*, d^*) is a steady state (a critical point of V_f) if and only if there exists $\theta^* \in \Theta$ with $J(\theta^*) = 0$. The corresponding $u^* \in (0,1]$ is given by*

$$u^* = \frac{R(\theta^*) - A(\theta^*)}{B(\theta^*)} \quad \text{if } B(\theta^*) \neq 0, \qquad \text{or} \quad u^* \text{ solves } u^2 - u + C(\theta^*) = 0 \text{ if } \theta^* = \theta_1,$$

  and then $d^* = -d_0 \ln u^*$, $L^* = 2W\sin(\theta^*/2)$. Moreover, the total number of steady states is at most two.
- *Generically (i.e. excluding parameter values where a zero of J also satisfies $J'(\theta) = 0$), the number is 0 or 2. A single steady state occurs only in degenerate situations: either a tangency with $J(\theta) = J'(\theta) = 0$ on one side of θ_1, or at the centre when*

$$k_\theta(\theta_1 - \theta_0) = F\,W\cos\Big(\frac{\theta_1}{2}\Big), \tag{C 1}$$

  and $D(\theta_1) = 2Fd_0$.
- *If the centre condition (C 1) holds and $D(\theta_1) > 2Fd_0$, then $\theta^* = \theta_1$ solves $J = 0$ and both quadratic roots $u_\pm$ of $u^2 - u + C(\theta_1) = 0$ are admissible; thus there are two distinct steady states with the same extension $L^* = 2W\sin(\theta_1/2)$ but different separations.*

Proof (sketch). From $\partial_d V_f = 0$ one obtains $u(1-u) = C(\theta)$ with $u = \mathrm{e}^{-d/d_0} \in (0,1]$, hence $\theta \in \Theta$. Using $\Phi(d) = u^2 - 2u = -(C(\theta) + u)$, the condition $\partial_L V_f = 0$ reduces to $A(\theta) + B(\theta)u = R(\theta)$. Eliminating u yields $J(\theta) = 0$; conversely, $J(\theta^*) = 0$ with $\theta^* \in \Theta$ reconstructs u^*, then d^*, L^*. At θ_1 and at the admissible endpoints $\theta_\pm$ one finds $J \leq 0$. Writing $G = R - A$, one has $J = -G^2 + GB - CB^2 \leq J_{\max} := B^2(1/4 - C)$, with $J_{\max} > 0$ iff $D(\theta) > 2Fd_0$. On each side of θ_1, $J_{\max}$ is unimodal (product of a single-hump factor $\varepsilon^2\mathrm{e}^{-\varepsilon^2/(2\sigma^2)}$, $\varepsilon = \theta - \theta_1$, and a strictly decreasing factor $\frac{D}{4} - \alpha$), vanishing at side endpoints; thus J can cross the axis at most once per side, giving the at most two bound. The one-solution cases follow from tangency $J = J' = 0$ on a side or from the centre condition together with the threshold $D(\theta_1) = 2Fd_0$. If $D(\theta_1) > 2Fd_0$ under (C 1), both $u_\pm$ are admissible at θ_1, producing two solutions with the same L. □

Proposition C.1 (Critical force). *Let $F_c := \frac{D_0}{2d_0}$. If $F > F_c$, then $\Theta = \varnothing$ and there are no steady states. If $0 \leq F \leq F_c$, the number of steady states is at most two.*

We now classify local stability of interior stationary points via the Hessian.

Theorem C.2 (Local stability at interior stationary points). *Let $V_f(L,d)$ be the free energy (2.7) on the interior domain $(L,d) \in (0,2W)\times(0,\infty)$, with parameters $k_\theta, D_0, d_0 > 0$. Assume $D(\theta) \in C^2$ and $\theta(L) = 2\arcsin(L/2W) \in C^2$. Let (L^*, d^*) be an interior stationary point:*

$$\partial_d V_f(L^*, d^*) = 0, \qquad \partial_L V_f(L^*, d^*) = 0.$$

Set $u^* := \mathrm{e}^{-d^*/d_0}$, $\theta^* := \theta(L^*)$, and evaluate at (L^*, d^*):

$$\theta' = \theta'(L^*), \quad \theta'' = \theta''(L^*), \quad D = D(\theta^*), \quad D' = \tfrac{\mathrm{d}D}{\mathrm{d}\theta}(\theta^*), \quad D'' = \tfrac{\mathrm{d}^2D}{\mathrm{d}\theta^2}(\theta^*), \quad \Phi = \Phi(d^*).$$

With variable order (L,d), the Hessian reads

$$H^* = \begin{bmatrix} \theta''\,\dfrac{F}{\theta'} + \theta'^2\big(k_\theta + \Phi\, D''\big) & \theta'\,F\,\dfrac{D'}{D} \\[2ex] \theta'\,F\,\dfrac{D'}{D} & \dfrac{2D}{d_0^2}\,u^*(2u^* - 1) \end{bmatrix}.$$

(i) Necessary curvature in d.

$$H^*_{dd} > 0 \iff u^* > \tfrac{1}{2} \iff d^* < d_0 \ln 2.$$

Downloaded from royalsocietypublishing.org/rsos/article-pdf/doi/10.1098/rsos.252316/6163680/rsos.252316.pdf
by guest
on 02 September 2026

Hence only the near branch $u^* > 1/2$ can be stable along d.

(ii) Strict local minimum (classification). *For a symmetric 2×2 Hessian, positive definiteness is equivalent to the positivity of the first leading principal minor and of the determinant (see standard matrix analysis texts, e.g. [102]):*

$$\boxed{H^*_{dd} > 0 \quad \textit{and} \quad \det H^* := H^*_{LL} H^*_{dd} - (H^*_{Ld})^2 > 0}.$$

If $H^*_{dd} > 0$ but $\det H^* < 0$ the point is a saddle; if $H^*_{dd} < 0$ it is unstable along d.

(iii) Zero force *$F = 0$. The stationary point is $(\bar{L}, 0)$ with $\bar{\theta} = \theta(\bar{L})$ solving $k_\theta(\bar{\theta} - \theta_0) = D'(\bar{\theta})$; it is locally stable iff*

$$k_\theta - D''(\bar{\theta}) > 0,$$

since $H_{dd} = 2D(\bar{\theta})/d_0^2 > 0$ and $H_{Ld} = 0$.

Fold remark. *At $u^* = 1/2$, $H^*_{dd} = 0$ and $\det H^* = -(H^*_{Ld})^2 \le 0$; thus no strict local minimum occurs exactly at the fold.*

Corollary C.1 (Sign structure on the d-stationary branch)**.** *Along the d-stationary branch, the first-order condition*

$$\frac{2}{d_0}\, u^*(1 - u^*) = \frac{F}{D(\theta^*)}$$

implies

$$\det H^*(L^*, d^*) = \frac{F}{d_0}\, S(L^*, u^*)\, s(u^*) - K(L^*),$$

where

$$s(u) = \frac{2u - 1}{1 - u}, \qquad K(L) = (\theta'(L)\, F)^2 \left(\frac{D'(\theta(L))}{D(\theta(L))} \right)^2 \ge 0,$$

$$S(L, u) = \frac{\theta''(L)\, F}{\theta'(L)} + \big(\theta'(L)\big)^2 \Big(k_\theta + \Phi(d)\, D''(\theta(L)) \Big).$$

Consequently:

- *If $S(L^*, u^*)$ and $s(u^*)$ have opposite signs, then $\det H^* < 0$ (saddle).*
- *On the near branch $u^* > 1/2$ (so $s > 0$), a strict local minimum requires*

$$S(L^*, u^*) > \frac{K(L^*)}{(F/d_0)\, s(u^*)}.$$

At the fold $u^* = 1/2$, $s = 0$ and $\det H^* = -K \le 0$, hence no strict local minimum there.

References

1. Rudolph MG, Stanfield RL, Wilson IA. 2006 How TCRs bind MHCs, peptides, and coreceptors. *Annu. Rev. Immunol.* **24**, 419–466. (doi:10.1146/annurev.immunol.23.021704.115658)
2. Sundberg EJ, Mariuzza RA. 2002 Molecular recognition in antibody-antigen complexes. *Adv. Protein Chem.* **61**, 119–160. (doi:10.1016/s0065-3233(02)61004-6)
3. Rossjohn J, Gras S, Miles JJ, Turner SJ, Godfrey DI, Mccluskey J. 2015 T cell antigen receptor recognition of antigen-presenting molecules. *Annu. Rev. Immunol.* **33**, 169–200. (doi:10.1146/annurev-immunol-032414-112334)
4. Huang J, Brameshuber M, Zeng X, Xie J, Li QJ, Chien YH, Valitutti S, Davis MM. 2013 A single peptide-major histocompatibility complex ligand triggers digital cytokine secretion in CD4(+) T cells. *Immunity* **14**, 846–857. (doi:10.1016/j.immuni.2013.08.036)
5. Brazin KN, Mallis RJ, Das DK, Feng Y, Hwang W, Wang JH, Wagner G, Lang MJ, Reinherz EL. 2015 Structural features of the $\alpha\beta$ TCR mechanotransduction apparatus that promote pMHC discrimination. *Front. Immunol.* **6**, 441 (doi:10.3389/fimmu.2015.00441)
6. Das DK *et al*. 2015 Force-dependent transition in the T-cell receptor beta-subunit allosterically regulates peptide discrimination and pMHC bond lifetime. *Proc. Natl Acad. Sci. USA* **112**, 1517–1522. (doi:10.1073/pnas.1424829112)
7. Lanz AL *et al*. 2021 Allosteric activation of T cell antigen receptor signaling by quaternary structure relaxation. *Cell Rep.* **36**, 109531. (doi:10.1016/j.celrep.2021.109375)
8. Mckeithan TW. 1995 Kinetic proofreading in T-cell receptor signal transduction. *Proc. Natl Acad. Sci. USA* **92**, 5042–5046. (doi:10.1073/pnas.92.11.5042)

Downloaded from royalsocietypublishing.org/rsos/article-pdf/doi/10.1098/rsos.252316/6163680/rsos.252316.pdf
by guest
on 02 September 2026

9. Davis SJ, Merwe PAVD. 2006 The kinetic-segregation model: TCR triggering and beyond. *Nat. Immunol.* **7**, 803–809. (doi:10.1038/ni1369)
10. Chang VT *et al*. 2016 Initiation of T cell signaling by CD45 segregation at 'close contacts'. *Nat. Immunol.* **17**, 574–582. (doi:10.1038/ni.3392)
11. Razvag Y, Neve-Oz Y, Sajman J, Reches M, Sherman E. 2018 Nanoscale kinetic segregation of TCR and CD45 in engaged microvilli facilitates early T cell activation. *Nat. Commun.* **9**, 732. (doi:10.1038/s41467-018-03127-w)
12. Cuendet MA, Michielin O. 2008 Protein-protein interaction investigated by steered molecular dynamics: the TCR-pMHC complex. *Biophys. J.* **95**, 3575–3590. (doi:10.1529/biophysj.108.131383)
13. Armstrong KM, Piepenbrink KH, Baker BM. 2008 Conformational changes and flexibility in T-cell receptor recognition of peptide-MHC complexes. *Biochem. J.* **415**, 183–196. (doi:10.1042/BJ20080850)
14. Klotzsch E, Schütz GJ. 2013 Improved ligand discrimination by force-induced unbinding of the T cell receptor from peptide-MHC. *Biophys. J.* **104**, 1670–1675. (doi:10.1016/j.bpj.2013.03.023)
15. Pettmann J *et al*. 2023 Mechanical forces impair antigen discrimination by reducing differences in T-cell receptor/peptide-MHC off-rates. *EMBO J.* **42**, 111841. (doi:10.15252/embj.2022111841)
16. St K, Takeuchi K, Sun ZY, Touma M, Castro CE, Fahmy A, Lang MJ, Wagner G, Reinherz EL. 2009 The $\alpha\beta$ T cell receptor is an anisotropic mechanosensor. *J. Biol. Chem.* **284**, 31 028–31 037. (doi:10.1074/jbc.M109.052712)
17. Lee MS, Glassman CR, Deshpande NR, Badgandi HB, Parrish HL, Uttamapinant C, Stawski PS, Ting AY, Kuhns MS. 2015 A mechanical switch couples T cell receptor triggering to the cytoplasmic juxtamembrane regions of CD3$\zeta\zeta$. *Immunity* **43**, 227–239. (doi:10.1016/j.immuni.2015.06.018)
18. Liu B, Chen W, Evavold BD, Zhu C. 2014 Accumulation of dynamic catch bonds between TCR and agonist peptide-MHC triggers T cell signaling. *Cell* **157**, 357–368. (doi:10.1016/j.cell.2014.02.053)
19. Ma R, Kellner AV, Ma VP, Su H, Deal BR, Brockman JM, Salaita K. 2019 DNA probes that store mechanical information reveal transient piconewton forces applied by T cells. *Proc. Natl Acad. Sci. USA* **116**, 16 949–16 954. (doi:10.1073/pnas.1904034116)
20. Liu Y, Blanchfield L, Ma VP, Andargachew R, Galior K, Liu Z, Evavold B, Salaita K. 2016 DNA-based nanoparticle tension sensors reveal that T-cell receptors transmit defined pN forces to their antigens for enhanced fidelity. *Proc. Natl Acad. Sci. USA* **113**, 5610–5615. (doi:10.1073/pnas.1600163113)
21. Choi HK *et al*. 2023 Catch bond models may explain how force amplifies TCR signaling and antigen discrimination. *Nat. Commun.* **14**, 2616. (doi:10.1038/s41467-023-38267-1)
22. Feng Y, Brazin KN, Kobayashi E, Mallis RJ, Reinherz EL, Lang MJ. 2017 Mechanosensing drives acuity of $\alpha\beta$ T-cell recognition. *Proc. Natl Acad. Sci. USA* **114**, E8204–E8213 (doi:10.1073/pnas.1703559114)
23. Hogquist KA, Jameson SC, Heath WR, Howard JL, Bevan MJ, Carbone FR. 1994 T cell receptor antagonist peptides induce positive selection. *Cell* **76**, 17–27. (doi:10.1016/0092-8674(94)90169-4)
24. Sibener LV *et al*. 2018 Isolation of a structural mechanism for uncoupling T cell receptor signaling from peptide-MHC binding. *Cell* **174**, 27. (doi:10.1016/j.cell.2018.06.017)
25. Puech PH, Bongrand P. 2021 Mechanotransduction as a major driver of cell behaviour: mechanisms, and relevance to cell organization and future research. *Open Biol.* **11**, 210256. (doi:10.1098/rsob.210256)
26. Sokurenko EV, Vogel V, Thomas WE. 2008 Catch-bond mechanism of force-enhanced adhesion: counterintuitive, elusive, but…widespread? *Cell Host Microbe* **4**, 314–323. (doi:10.1016/j.chom.2008.09.005)
27. Chen KY *et al*. 2021 Trapping or slowing the diffusion of T cell receptors at close contacts initiates T cell signaling. *Proc. Natl Acad. Sci. USA* **118**, 2024250118. (doi:10.1073/pnas.2024250118)
28. Natarajan K *et al*. 2017 An allosteric site in the T-cell receptor Cβ domain plays a critical signalling role. *Nat. Commun.* **8**, 15260. (doi:10.1038/ncomms15260)
29. He Y, Agnihotri P, Rangarajan S, Chen Y, Kerzic MC, Nussinov R, Mariuzza RA, Orban J. 2020 Peptide-MHC binding reveals conserved allosteric sites in MHC class I- and class II-restricted T cell receptors (TCRs). *J. Mol. Biol.* **432**, 166697. (doi:10.1016/j.jmb.2020.10.031)
30. Starr TK, Jameson SC, Hogquist KA. 2003 Positive and negative selection of T cells. *Annu. Rev. Immunol.* **21**, 139–176. (doi:10.1146/annurev.immunol.21.120601.141107)
31. Hong J *et al*. 2018 TCR mechanotransduction signaling loop induces negative selection in the thymus. *Nat. Immunol.* **19**, 1379–1390. (doi:10.1038/s41590-018-0259-z)
32. Stepanek O *et al*. 2014 Coreceptor scanning by the T cell receptor provides a mechanism for T cell tolerance. *Cell* **159**, 333–345. (doi:10.1016/j.cell.2014.08.042)
33. Xu C, Gagnon E, Call ME, Schnell JR, Schwieters CD, Carman CV, Chou JJ, Wucherpfennig KW. 2008 Regulation of T cell receptor activation by dynamic membrane binding of the CD3 epsilon cytoplasmic tyrosine-based motif. *Cell* **135**, 702–713. (doi:10.1016/j.cell.2008.09.044)
34. Deford-Watts LM, Tassin TC, Becker AM, Medeiros JJ, Albanesi JP, Love PE, Wülfing C, Oers NSV. 2009 The cytoplasmic tail of the T cell receptor CD3 epsilon subunit contains a phospholipid-binding motif that regulates T cell functions. *J. Immunol.* **183**, 1055–1064. (doi:10.4049/jimmunol.0900404)
35. Zhang H, Cordoba SP, Dushek O, Merwe PAVD. 2011 Basic residues in the T-cell receptor ζ cytoplasmic domain mediate membrane association and modulate signaling. *Proc. Natl Acad. Sci. USA* **108**, 19 323–19 328. (doi:10.1073/pnas.1108052108)

Downloaded from royalsocietypublishing.org/rsos/article-pdf/doi/10.1098/rsos.252316/6163680/rsos.252316.pdf
by guest
on 02 September 2026

36. Fernández-Aguilar LM, Vico-Barranco I, Arbulo-Echevarria MM, Aguado E. 2023 A story of kinases and adaptors: the role of Lck, ZAP-70 and LAT in switch panel governing T-cell development and activation. *Biology* **12**, 1163. (doi:10.3390/biology12091163)
37. Stachowiak JC, Brodsky FM, Miller EA. 2013 A cost-benefit analysis of the physical mechanisms of membrane curvature. *Nat. Cell Biol.* **15**, 1019–1027. (doi:10.1038/ncb2832)
38. Stachowiak JC, Schmid EM, Ryan CJ, Ann HS, Sasaki DY, Sherman MB, Geissler PL, Fletcher DA, Hayden CC. 2012 Membrane bending by protein-protein crowding. *Nat. Cell Biol.* **14**, 944–949. (doi:10.1038/ncb2561)
39. Keskin O. 2007 Binding induced conformational changes of proteins correlate with their intrinsic fluctuations: a case study of antibodies. *BMC Struct. Biol.* **7**, 31. (doi:10.1186/1472-6807-7-31)
40. Guo S, Efremov AK, Yan J. 2019 Understanding the catch-bond kinetics of biomolecules on a one-dimensional energy landscape. *Commun. Chem.* **2**, 30. (doi:10.1038/s42004-019-0131-6)
41. Ayres CM, Corcelli SA, Baker BM. 2023 The energetic landscape of catch bonds in TCR interfaces. *J. Immunol.* **211**, 325–332. (doi:10.4049/jimmunol.2300121)
42. Mariuzza RA, Agnihotri P, Orban J. 2020 The structural basis of T-cell receptor (TCR) activation: an enduring enigma. *J. Biol. Chem.* **295**, 914–925. (doi:10.1074/jbc.REV119.009411)
43. Merwe PAVD, Davis SJ. 2003 Molecular interactions mediating T cell antigen recognition. *Annu. Rev. Immunol.* **21**, 659–684. (doi:10.1146/annurev.immunol.21.120601.141036)
44. Wilson IA, Garcia KC. 1997 T-cell receptor structure and TCR complexes. *Curr. Opin. Struct. Biol.* **7**, 839–848. (doi:10.1016/s0959-440x(97)80156-x)
45. Hera ADL, Müller U, Olsson C, Isaaz S, Tunnacliffe A. 1991 Structure of the T cell antigen receptor (TCR): two CD3 epsilon subunits in a functional TCR/CD3 complex. *J. Exp. Med.* **173**, 7–17. (doi:10.1084/jem.173.1.7)
46. Saotome K *et al*. 2023 Structural analysis of cancer-relevant TCR-CD3 and peptide-MHC complexes by cryoEM. *Nat. Commun.* **14**, 2401. (doi:10.1038/s41467-023-37532-7)
47. Eerden FJV, Alrahman LCMSA, Anais M, Arthur L, Xiuyuan I, Shigenari Y, Sho S, Daron M. 2023 TCR-pMHC complex formation triggers CD3 dynamics. *eLife* **12**, RP88065. (doi:10.7554/eLife.88065.1)
48. Al-Aghbar MA, Jainarayanan AK, Dustin ML, Roffler SR. 2022 The interplay between membrane topology and mechanical forces in regulating T cell receptor activity. *Commun. Biol.* **5**, 40. (doi:10.1038/s42003-021-02995-1)
49. Pandey PR, Różycki B, Lipowsky R, Weikl TR. 2021 Structural variability and concerted motions of the T cell receptor–CD3 complex. *eLife* **10**, e67195. (doi:10.7554/eLife.67195)
50. Dong D *et al*. 2019 Structural basis of assembly of the human T cell receptor-CD3 complex. *Nature* **573**, 546–552. (doi:10.1038/s41586-019-1537-0)
51. Reinherz EL. 2019 The structure of a T-cell mechanosensor. *Nature* **573**, 502–504. (doi:10.1038/d41586-019-02646-w)
52. He Y *et al*. 2015 Identification of the docking site for CD3 on the T cell receptor β chain by solution NMR. *J. Biol. Chem.* **290**, 19 796–19 805. (doi:10.1074/jbc.M115.663799)
53. Prakaash D, Cook GP, Acuto O, Kalli AC. 2021 Multi-scale simulations of the T cell receptor reveal its lipid interactions, dynamics and the arrangement of its cytoplasmic region. *PLoS Comput. Biol.* **17**, 1009232. (doi:10.1371/journal.pcbi.1009232)
54. Barkan CO, Bruinsma RF. 2024 Topology of molecular deformations induces triphasic catch bonding in selectin-ligand bonds. *Proc. Natl Acad. Sci. USA* **121**, 2315866121. (doi:10.1073/pnas.2315866121)
55. Quapp W, Bofill JM, Ribas-Ariño J. 2018 Toward a theory of mechanochemistry: simple models from the very beginnings. *Int. J Quantum Chem.* **118**, e25775. (doi:10.1002/qua.25775)
56. Quapp W, Bofill JM. 2018 Mechanochemistry on the Müller-Brown surface by Newton trajectories. *Int. J Quantum Chem.* **118**, e25522. (doi:10.1002/qua.25522)
57. Quapp W, Bofill JM. 2024 Theory and examples of catch bonds. *J. Phys. Chem. B* **128**, 4097–4110. (doi:10.1021/acs.jpcb.4c00468)
58. Quapp W, Bofill JM. 2016 Reaction rates in a theory of mechanochemical pathways. *J. Comput. Chem.* **37**, 2467–2478. (doi:10.1002/jcc.24470)
59. Konda SS, Brantley JN, Varghese BT, Wiggins KM, Bielawski CW, Makarov DE. 2013 Molecular catch bonds and the anti-Hammond effect in polymer mechanochemistry. *J. Am. Chem. Soc.* **135**, 12 722–12 729. (doi:10.1021/ja4051108)
60. Suzuki Y, Dudko OK. 2011 Biomolecules under mechanical stress: a simple mechanism of complex behavior. *J. Chem. Phys.* **134**, 65102. (doi:10.1063/1.3533366)
61. Thomas WE. 2007 Understanding the counterintuitive phenomenon of catch bonds. *Curr. Nanosci.* **3**, 63–77. (doi:10.2174/157341307779940544)
62. Wu P *et al*. 2019 Mechano-regulation of peptide-MHC class I conformations determines TCR antigen recognition. *Mol. Cell* **73**, 1015–1027. (doi:10.1016/j.molcel.2018.12.018)
63. Sušac L *et al*. 2022 Structure of a fully assembled tumor-specific T cell receptor ligated by pMHC. *Cell* **185**, 3201–3213.e19. (doi:10.1016/j.cell.2022.07.010)

Downloaded from royalsocietypublishing.org/rsos/article-pdf/doi/10.1098/rsos.252316/6163680/rsos.252316.pdf
by guest
on 02 September 2026

64. Quapp W, Bofill JM, Ribas-Ariño J. 2017 Analysis of the acting forces in a theory of catalysis and mechanochemistry. *J. Phys. Chem. A* **121**, 2820–2838. (doi:10.1021/acs.jpca.7b00022)
65. Hratchian HP, Schlegel HB. 2005 Finding minima, transition states, and following reaction pathways on ab initio potential energy surfaces. In *Theory and applications of computational chemistry* (eds CE Dykstra, G Frenking, KS Kim, GE Scuseria), pp. 195–249. Amsterdam, The Netherlands: Elsevier. (doi:10.1016/B978-044451719-7/50053-6)
66. Chakrabarti S, Hinczewski M, Thirumalai D. 2014 Plasticity of hydrogen bond networks regulates mechanochemistry of cell adhesion complexes. *Proc. Natl Acad. Sci. USA* **111**, 9048–9053. (doi:10.1073/pnas.1405384111)
67. Adhikari S, Moran J, Weddle C, Hinczewski M. 2018 Unraveling the mechanism of the cadherin-catenin-actin catch bond. *PLoS Comput. Biol.* **14**, 1006399. (doi:10.1371/journal.pcbi.1006399)
68. Evans E, Ritchie K. 1997 Dynamic strength of molecular adhesion bonds. *Biophys. J.* **72**, 1541–1555. (doi:10.1016/S0006-3495(97)78802-7)
69. Thomas WE, Vogel V, Sokurenko E. 2008 Biophysics of catch bonds. *Annu. Rev. Biophys.* **37**, 399–416. (doi:10.1146/annurev.biophys.37.032807.125804)
70. Diener I, Schaback R. 1990 An extended continuous Newton method. *J. Optim. Theory Appl.* **67**, 77. (doi:10.1007/BF00939735)
71. Xie N, Bompard E, Napoli R, Torelli F. 2012 Widely convergent method for finding solutions of simultaneous nonlinear equations. *Electr. Power Syst. Res.* **83**, 9–18. (doi:10.1016/j.epsr.2011.09.002)
72. Quapp W, Hirsch M, Imig O, Heidrich D. 1998 Searching for saddle points of potential energy surfaces by following a reduced gradient. *J. Comput. Chem.* **19**, 1087–1100. (doi:10.1002/(SICI)1096-987X(19980715)19:9<1087::AID-JCC9>3.3.CO;2-S)
73. Quapp W, Hirsch M, Heidrich D. 1998 Bifurcation of reaction pathways: the set of valley ridge inflection points of a simple three-dimensional potential energy surface. *Theor. Chem. Acc.* **100**, 285–299. (doi:10.1007/s002140050389)
74. Hirsch M, Quapp W. 2004 The reaction pathway of a potential energy surface as curve with induced tangent. *Chem. Phys. Lett.* **395**, 150–156. (doi:10.1016/j.cplett.2004.07.079)
75. Bell GI. 1978 Models for the specific adhesion of cells to cells. *Science* **200**, 618–627. (doi:10.1126/science.347575)
76. Howard J. 2001 *Mechanics of motor proteins and the cytoskeleton*. Sunderland, MA: Sinauer Associates.
77. Morse PM. 1929 Diatomic molecules according to the wave mechanics. II. Vibrational levels. *Phys. Rev.* **34**, 57–64. (doi:10.1103/PhysRev.34.57)
78. Hill TL. 2005 *Free energy transduction and biochemical cycle kinetics*. Mineola, NY: Dover Publications.
79. Tian S, Maile R, Collins EJ, Frelinger JA. 2007 $CD8^+$ T cell activation is governed by TCR-peptide/MHC affinity, not dissociation rate. *J. Immunol.* **179**, 2952–2960. (doi:10.4049/jimmunol.179.5.2952)
80. Alam SM, Davies GM, Lin CM, Zal T, Nasholds W, Jameson SC, Hogquist KA, Gascoigne NR, Travers PJ. 1999 Qualitative and quantitative differences in T cell receptor binding of agonist and antagonist ligands. *Immunity* **10**, 227–237. (doi:10.1016/s1074-7613(00)80023-0)
81. Boulter JM, Schmitz N, Sewell AK, Godkin AJ, Bachmann MF, Gallimore AM. 2007 Potent T cell agonism mediated by a very rapid TCR/pMHC interaction. *Eur. J. Immunol.* **37**, 798–806. (doi:10.1002/eji.200636743)
82. Chang-Gonzalez AC, Mallis RJ, Lang MJ, Reinherz EL, Hwang W. 2023 Asymmetric framework motion of TCR$\alpha\beta$ controls load-dependent peptide discrimination. *bioRxiv*. (doi:10.1101/2023.09.10.557064)
83. Hill TL. 2013 *Cooperativity theory in biochemistry: steady-state and equilibrium systems*. New York, NY: Springer.
84. Dill KA. 1990 Dominant forces in protein folding. *Biochemistry* **29**, 7133–7155. (doi:10.1021/bi00483a001)
85. Gilson MK, Given JA, Bush BL, Mccammon JA. 1997 The statistical-thermodynamic basis for computation of binding affinities: a critical review. *Biophys. J.* **72**, 1047–1069. (doi:10.1016/S0006-3495(97)78756-3)
86. Pettersen EF, Goddard TD, Huang CC, Couch GS, Greenblatt DM, Meng EC, Ferrin TE. 2004 UCSF chimera—a visualization system for exploratory research and analysis. *J. Comput. Chem.* **25**, 1605–1612. (doi:10.1002/jcc.20084)
87. National Library of Medicine. 2024 Technical report. Molecular modeling database (MMDB). See https://www.ncbi.nlm.nih.gov/Structure/.
88. Garboczi DN, Ghosh P, Utz U, Fan QR, Biddison WE, Wiley DC. 1996 Structure of the complex between human T-cell receptor, viral peptide and HLA-A2. *Nature* **384**, 134–141. (doi:10.1038/384134a0)
89. Friddle RW, Noy A, Yoreo JJD. 2012 Interpreting the widespread nonlinear force spectra of intermolecular bonds. *Proc. Natl Acad. Sci. USA* **109**, 13 573–13 578. (doi:10.1073/pnas.1202946109)
90. Langley JN. 1905 On the reaction of cells and of nerve-endings to certain poisons, chiefly as regards the reaction of striated muscle to nicotine and to curari. *J. Physiol.* **33**, 374–413. (doi:10.1113/jphysiol.1905.sp001128)
91. Clark AJ. 1926 The reaction between acetyl choline and muscle cells. *J. Physiol.* **61**, 530–546. (doi:10.1113/jphysiol.1926.sp002314)
92. Stephenson RP. 1956 A modification of receptor theory. *Br. J. Pharmacol. Chemother.* **11**, 379–393. (doi:10.1111/j.1476-5381.1956.tb00006.x)
93. Ariens EJ. 1954 Affinity and intrinsic activity in the theory of competitive inhibition. I. Problems and theory. *Arch. Int. Pharmacodyn. Ther.* **99**, 32–49.
94. Arunlakshana O, Schild HO, Jenkinson DH. 1997 Some quantitative uses of drug antagonists. *Br. J. Pharmacol.* **120**, 148–150. (doi:10.1111/j.1476-5381.1997.tb06792.x)

Downloaded from royalsocietypublishing.org/rsos/article-pdf/doi/10.1098/rsos.252316/6163680/rsos.252316.pdf
by guest
on 02 September 2026

95. Arrhenius S. 1889 Über die Reaktionsgeschwindigkeit bei der Inversion von Rohrzucker durch Säuren. *Z. Phys. Chem.* **4**, 226–248. (doi:10.1515/zpch-1889-0416)
96. Kramers HA. 1940 Brownian motion in a field of force and the diffusion model of chemical reactions. *Physica* **7**, 284–304. (doi:10.1016/S0031-8914(40)90098-2)
97. Hänggi P, Talkner P, Borkovec M. 1990 Reaction-rate theory: fifty years after Kramers. *Rev. Mod. Phys.* **62**, 251–341. (doi:10.1103/RevModPhys.62.251)
98. Langer JS. 1969 Statistical theory of the decay of metastable states. *Ann. Phys.* **54**, 258–275. (doi:10.1016/0003-4916(69)90153-5)
99. Mckay MD, Beckman RJ, Conover WJ. 2000 A comparison of three methods for selecting values of input variables in the analysis of output from a computer code. *Technometrics* **42**, 55–61. (doi:10.1080/00401706.2000.10485979)
100. Marino S, Hogue IB, Ray CJ, Kirschner DE. 2008 A methodology for performing global uncertainty and sensitivity analysis in systems biology. *J. Theor. Biol.* **254**, 178–196. (doi:10.1016/j.jtbi.2008.04.011)
101. Qin R *et al*. 2025 TCR catch bonds nonlinearly control CD8 cooperation to shape T cell specificity. *Cell Res.* **35**, 265–283. (doi:10.1101/2025.11.15.688643)
102. Horn RA, Johnson CR. 2012 *Matrix analysis*. Cambridge, UK. Cambridge University Press.

Downloaded from royalsocietypublishing.org/rsos/article-pdf/doi/10.1098/rsos.252316/6163680/rsos.252316.pdf
by guest
on 02 September 2026